Master's Thesis : An in-silico modelling platform for the prediction of Posterior Vault Expansion outcomes

Auteur : Deliège, Lara
Promoteur(s) : Geris, Liesbet
Faculté : Faculté des Sciences appliquées
Diplôme : Master en ingénieur civil biomédical, à finalité spécialisée
Année académique : 2019-2020
URI/URL : http://hdl.handle.net/2268.2/9078

SPRING ASSISTED CRANIOPLASTY :

An in-silico modelling platform for the prediction of Posterior Vault Expansion outcomes.

Master thesis conducted by

LARA DELIEGE

with the aim of obtaining the degree of Master in Biomedical Engineering

Under the supervision of

Dr. Liesbet Geris
Dr. Alessandro Borghi
Dr. Silvia Schievano

University of Liege - Faculty of Applied Sciences
ACADEMIC YEAR 2019-2020

Abstract

Posterior Vault Expansion using springs (PVE) has been adopted at Great Ormond Street Hospital (GOSH) with the aim of normalizing deformed head shapes. These calvarial abnormalities are caused by a birth defect called craniosynostosis. This condition causes the fusion of certain skull sutures before birth and can generate high intracranial pressure when the brain starts developing. The goal of surgical correction is to normalize the head shape by means of metallic distractors (springs) which expand the back portion of the skull and increase the intracranial volume. In case of sagittal craniosynostosis correction, it has been shown that surgical outcomes can be predicted numerically using the finite element method (FEM): we hereby tested such method for the prediction of PVE surgical outcomes using information retrievable from Computed Tomography (CT) scans and X-ray images.

Fourteen patients who underwent PVE (age at surgery= 2.0 ± 1.7 years, range [5 months ; 5.5 years]) who received preoperative CT (± 44 days before surgery) and postoperative CT (± 147 days after surgery) were recruited. Seven of these patients were treated using two springs (same model - either S10, S12 or S14), five with four and two with six springs. Information on osteotomies and location of spring attachments were recovered from the postoperative CTs. Springs expansion was simulated over 10 days in `Ansys Mechanical 19 R1`. Simulated skull shapes were retrieved and compared with postoperative CT images. For each patient, Intracranial Volume (ICV) and Cranial Index (CI) were also computed. Finally, the spring kinematics was updated using X-ray images of a database of 50 patients. The springs dimensions were manually measured for each of them and recorded to update the material properties in order to reflect a different expansion kinematics.

The average postoperative ICV recorded was 1.45 L ± 0.23 L and the simulated model yielded comparable values with an average of 1.39 L ± 0.24 L. The average postoperative CI recovered from CT scans was 87.8 ± 11.1% against 84.4 ± 12.4% for the model. Comparison of the simulated postoperative skull with the postoperative CT skull reconstruction showed very similar extent of expansion. It appeared that the springs involved in a PVE open more slowly than in the case of the sagittal procedure (67% of maximal opening reached after 21 days in opposition to 1 day, respectively).

Finite element modeling seems to be a suitable technique to predict the outcome of PVE with springs. Further developments will expand the model by including crack propagation, which occurs at the skull base in a subset of patients, therefore allowing for further improvement in modelling capability. The final goal of this project is to be able to use this patient-specific model (using data from 3D medical imaging) as a tool for surgical planning for spring assisted posterior vault expansion and improve the current understanding of the effect of surgical correction in patients affected by syndromic craniosynostosis.

Acknowledgements

This project represents my first experience of a long term work and I probably would not have been able to conclude it without the assistance and support of many.

First and foremost, I would like to express my gratitude to my promoter Professor Liesbet Geris for giving me the opportunity to work on this exciting project in London and being available whenever I needed help or advice.

Thereafter, I would like to thank my supervisors, Prof. Alessandro Borghi and Prof. Silvia Schievano from UCL for welcoming and including me in their researches. They have always been supportive and available to answer any of my questions. They also have been really encouraging and enthusiastic towards my work all along the way. I especially want to thank them for letting me borrow hardware before coming back home due to the covid-19 pandemic to continue my work in the best conditions possible. They have been really helpful and responsive via online meetings during this unusual situation.

Moreover, I would like to express my thanks to the people working in the team that made me feel welcome and at ease in the office. Everyone was ready to help and take time off their work to answers any questions or issues that I might have been facing at the time.

Finally, I am deeply grateful to my family and friends who encouraged me all along the ups and downs of the experience.

Table of contents

Introduction

The incidence of craniosynostosis worldwide is 1 in 2,000 to 2,500 live births each year [1]. This condition is defined as the deformation of skull growth associated with premature closure of one or more skull vault sutures. The spectrum of the disorder most commonly involves the closure of a single suture in the skull, but in case of syndromic craniosynostosis (where an underlying genetic abnormality is present) multiple sutures are affected and extra-cranial anomalies can be present. This condition, in advanced stages, presents a considerable risk for the development of the child's brain. Prematurely fused sutures don't allow the skull to properly expand as the brain is growing, resulting in elevated intracranial pressure (ICP) that could have detrimental consequences on the patient's life and development [1].

Until recently, procedures used to treat craniosynostosis carried a mortality rate of 1.5–2% and were associated with complications such as blood loss, infection, spontaneous cerebrospinal fluid (CSF) leak, and required lengthy hospital stay as well as post-operative monitoring in an intensive care unit [2]. In 2008, the spring assisted cranioplasty (SAC) was introduced at Great Ormond Street Hospital in London to treat patients affected by craniosynostosis. It is now the preferred minimally invasive technique as it allows the treatment of craniosynostosis at an early stage.

Surgical outcomes in terms of final head shape remain partially unpredictable as the spring placement is performed according to the operating surgeon's judgement. Therefore, the question we have decided to address is the following: would it be possible to predict the head shape after the spring cranioplasty procedure, depending on the osteotomy performed and the patient's own anatomical features, using an in-silico model?

This thesis is divided into six main chapters. The first one is dedicated to the definition of the general context of the project. The basic anatomy notions of the skull are introduced. Also, more details are given about the different types of craniosynostosis, existing syndromes and current treatment approaches. Afterwards, a quick introduction of the previous work is provided in order to introduce the main aim of this master thesis.

The second chapter focuses on the method of data pre-processing: how the models were retrieved by means of medical image segmentation and prepared for simulation as well as the set-up in *Ansys mechanical*.

Chapter three reports the results from the first set of simulations. Results are presented in three different ways: visually by overlaying post-op 3D models with simulated end-of-expansion FEA models, by comparison of the intracranial volumes (ICV, measured vs simulated) and by comparing a standard craniometric index (measured vs simulated). Method limitations are high-

lighted for a subset of patients.

The fourth chapter will concentrate on an optimization of the spring kinematics in order to tackle the aforementioned limitations.

Chapter five will then show that spring kinematics optimization improves modelling outcomes for the previously mentioned subset of patients and makes the overall model more efficient and robust.

Finally, the last chapter highlights the possible future works that were explored regarding the onset of fracture of the skull over time. This lead was followed using some hypotheses to model the crack propagation in a specific patient's skull.

Chapter 1

Background

The goal of this chapter is to provide a general context for the project. First, the basic structure and function of the skull will be described, starting from the bony tissue and then following with the membranous portions (cranial sutures). Then, we will review the current knowledge about the craniosynostosis (premature suture closure): syndromic or non-syndromic, the most common syndromes, their cause and consequences, finishing with a review of the techniques used to treat craniosynostosis. Afterwards, we will focus on the case of sagittal craniosynostosis patients. Finally, the main contributions of this master thesis are presented.

1.1 Anatomy

1.1.1 The Skull

The skull (or cranium) is the bony structure of the head. It supports the structures of the face and forms a cavity for the brain. Like the skulls of other vertebrates, it protects the brain from injury. Its functions also include fixing the distance between the eyes to allow stereoscopic vision, and fixing ears position to enable sound localisation in terms of direction and distance [3].
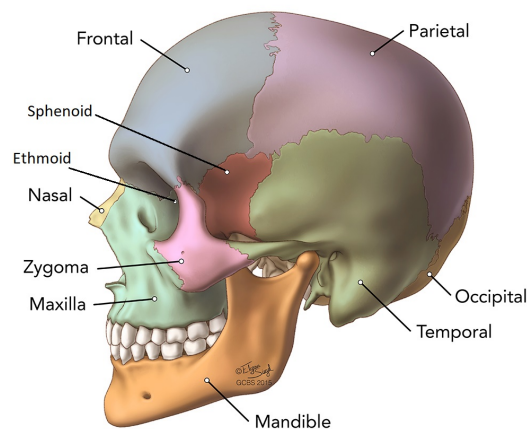
Figure 1.1: Lateral view of the skull bones

► **Skull Bones**

The skull is made up of 22 bones: the cranium includes eight bones, that forms the cavity for the brain (the occipital bone, two parietal bones, two temporal bones, the ethmoid, sphenoid and frontal bones), depicted on Figure 1.1. The 14 other bones compose the face and include the nasal bone, the zygomas and the maxilla bone. The mandible is the only moving part of the skull, it allows the opening and closing of the mouth [4].
Their macroscopic structure is common to other types of bone; they are composed of different layers:

- Periosteum: this is the outer surface of the bone. It contains blood vessels and nerves that help provide nutrients.

- Compact bone: this is the layer of bone below the periosteum. It's a very hard, dense type of bone tissue.

- Diploe: this is the innermost layer. It's lightweight and its spongy structure helps absorb sudden stress.

These layers together are the optimal combination to provide maximal strength and shock absorption at the same time (Figure 1.2) [5].
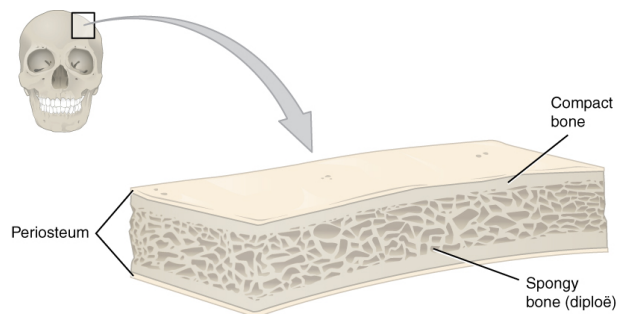
Figure 1.2: Structure of flat bones [5]

► **Sutures**

In babies, the edges of the skull bones are held together by soft tissue structures called "sutures", in order to form a structure that is both flexible and strong. The major sutures that will be addressed in this project are: the sagittal suture - junction between the two parietal bones - the coronal suture - junction between the frontal and parietal bones - the squamosal suture - junction between the parietal and temporal bones - and the lambdoid suture - junction between the parietal and occipital bones depicted in Figures 1.3 to 1.5. Sutures close over time to increase skull rigidity and improve resistance to trauma [6].
In newborns, the skull bones are linked by fibrous membranes called fontanelles (Figure 1.6). They allow the skull to be compressed during birth and then to accommodate to the growth of the brain during early infancy. It would usually takes 2 months for the posterior fontanelle to close while between 7 and 18 months for the closure of the anterior one [7] [8].

Figure 1.3: Sutures : superior view [4]

Figure 1.4: Sutures : posterior view [4]

Figure 1.5: Sutures : lateral view [4]

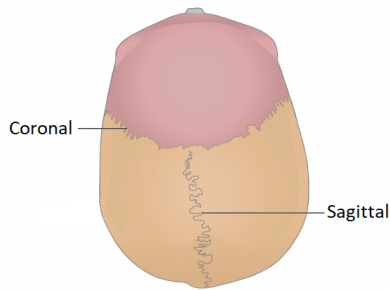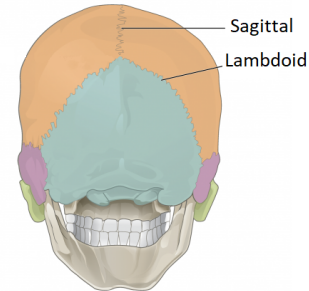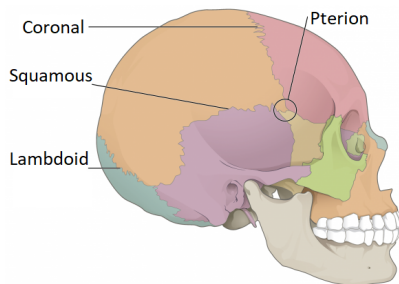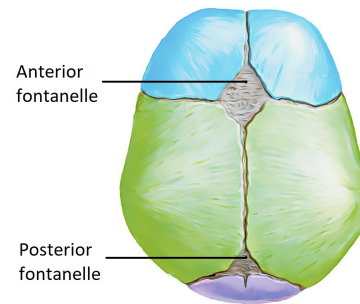Figure 1.6: Anterior and posterior fontanelles [9]

1.2   Bone Composition and Growth

As we know, bone is composed of three major components: an organic phase (30%), an inorganic phase (60%) and water (10%). The organic phase is mainly composed of collagen Type 1 (90%) which, organized in triple helix chains, provides tensile strength, proteoglycans and other noncollagenous proteins. The inorganic component is mainly made of calcium hydroxyapatite $Ca_{10}(PO_4)_6(OH)_2$ under the form of mineral plates placed between the collagen fibers. This combination of materials makes bone, a composite material. It will benefit the elasticity and toughness of the collagen fibers as well as the hardness and rigidity of the mineral plates [10].

Three types of cells are involved in the bone growth/remodeling; the osteoblasts, the osteocytes and the osteoclasts. Osteoblasts are bone-forming cells, osteocytes are mature bone cells and osteoclasts break down and reabsorb bone. There are two types of ossification: intramembranous and endochondral [11]. The first one consists in the substitution of connective tissue membranes with bony tissue. This phenomenon is characteristic of flat bones on top of the skull. The future bones begin their formation as connective tissue membranes (the fontanelles for example) then the osteoblasts migrate to the membranes and deposit bony matter around themselves. Once they are completely enclosed, they are called osteocytes. The second type of ossification involves the replacement of hyaline cartilage with bony tissues [11]. The first step consists in the infiltration of cartilage with blood vessels and osteoblasts that start to convert the cartilage into a periosteum, while enclosed cartilage is disintegrating and progressively leaving behind the medullary cavity [12]. In long bones, another center of bone growth appears later and is located in the epiphyses i.e. the extremities. At the end of ossification, only two areas still contain cartilage: the articular

cartilage over the epiphyses and the epiphyseal plate cartilage between the epiphysis and diaphysis (central part). The endocranium and the bones supporting the brain (the occipital, sphenoid, and ethmoid) are largely formed by endochondral ossification while frontal and parietal bones are intramembranous.[11]
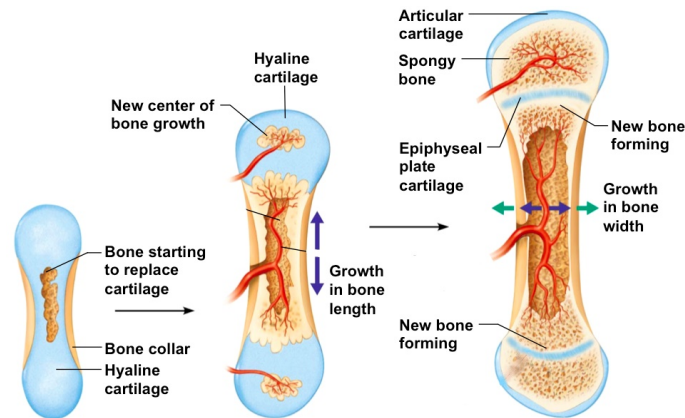
Figure 1.7: Schematic of bone formation [12]

1.3 Craniosynostosis

As mentioned before, craniosynostosis describes partial or complete premature fusion of cranial sutures. Craniosynostosis can be described as involving a single suture versus multiple sutures and as either syndromic or non-syndromic.

1.3.1 Non-syndromic craniosynostosis

This type of craniosynostosis is the most commonly encountered, it typically involves a single suture generally being sagittal, unicoronal, bicoronal, metopic or lambdoid. Sagittal synostosis is the most common form and represents about 45% of non-syndromic cases and results in an elongated shape of the head. Unicoronal synostosis is involved in 25% of cases resulting in an unilateral flattening of the forehead on the affected side. In contrast, bicoronal fusion produces skull shortening in the anterior-posterior direction and skull lengthening in the lateral directions. The metopic synostosis also occurs in 25% of cases [13]. It results in a triangular-shaped forehead and parietal and occipital prominence. Finally, the rarest forms of synostosis show the fusion of one lambdoid suture. This gives the skull an appearance of obliquity when viewed from behind [14]. All these cases are illustrated in Figure 1.8.

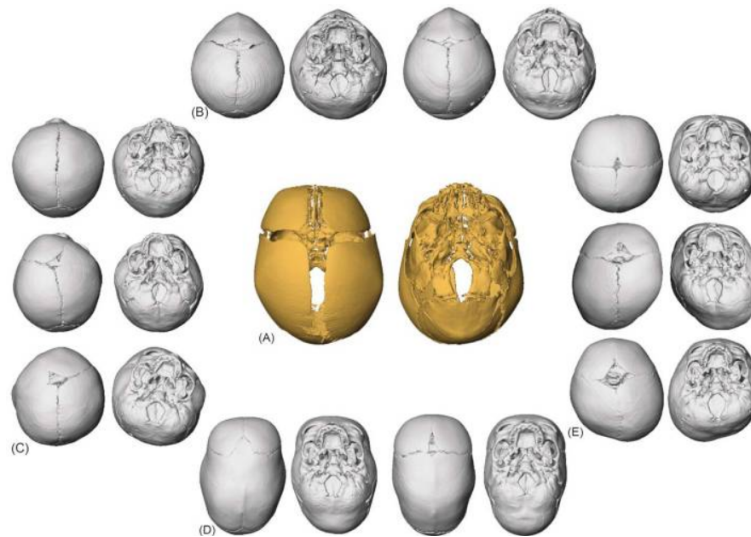Figure 1.8: Different cases of craniosynostosis presented from the superior and inferior views. (A) unaffected individual; (B) metopic craniosynostosis; (C) bicoronal craniosynostosis (top), right unicoronal craniosynostosis (center), left unicoronal craniosynostosis (bottom); (D) sagittal craniosynostosis; (E) bilateral lambdoid craniosynostosis (top), Right unilateral lambdoid craniosynostosis (center), and left unilateral lambdoid craniosynostosis (bottom). [15]

1.3.2 Syndromic

Patients with syndromic craniosynostosis have underlying genetic anomalies which make these patients much more complicated to care for. Those anomalies are well-defined and grouped in clinically recognisable syndromes. The syndromic craniosynostosis cases can demonstrate dominant, recessive and X-linked patterns of inheritance.

Many of the craniosynostosis syndromes are caused by mutations in the Fibroblast Growth Factor Receptors (FGFRs). FGFR-2 is the main gene of the family which also includes FGFR-1 and FGFR-3, and is involved in various syndromic craniosynostosis. However, FGFR-2 mutations show different clinical presentations and patients with the same mutation can exhibit diverse clinical manifestations. [2][16]

The most commonly identified syndromes include:

- *Apert syndrome* : this syndrome is generally characterized by bicoronal synostosis as well as a severe symmetrical syndactyly of fingers and toes. Syndactyly is a condition where two or more extremities (fingers or toes) are fused together (Figure 1.11). It is mainly caused by mutations in FGFR-2 that occurs in about 1 in 100,000 births. Cranial characteristics include a large anterior fontanelle, temporal widening and occipital flattening (Figure 1.10) [17][16].

- *Crouzon syndrome* : this condition shows 2 mains characteristics; brachycephaly (meaning that the skull is shorter than normal) and shallow orbits due to deficient anterior calvarial growth and early fusion of surrounding bones. The latter leads to an ocular proptosis which is a protrusion of the eye from its socket. It is caused by mutations in the FGFR-2 but as

opposed to Apert Syndrome, it usually isn't associated with limb abnormalities. The prevalence is 1 in 25,000 births, making it the most common syndromic craniosynostosis. The most usual pattern is bicoronal synostosis (brachycephaly) although scaphocephaly (elongated skull), trigonocephaly (triangular-shaped head) and even cloverleaf skull deformity have been recorded (Figure 1.9) [17][16].

- *Pfeiffer syndrome* : this syndrome has a range of features and presentations, making its severity range from mild to very severe. Usually, radially deviated thumbs and/or big toes in addition to turribrachycephaly (head elongated upwards) are observed. The majority of the cases involve mutations of FGFR-2 but also of FGFR-1. The incidence is about 1 in 100,000 live births. The Pfeiffer syndrome can be classified in three clinical sub-types: Type 1 is the classic one with the features described above, Type 2 and Type 3 are more severe ones such as cloverleaf skull (only in Type 3) (Figure 1.12) [17][16].

- *Saethre-Chotzen syndrome* : this condition usually involves unilateral or bilateral coronal synostosis. It is caused by the autosomal-dominant inheritance of mutations of TWIST-1, a transcription factor that is responsible for mesenchymal cell development of the cranium. Some characteristic features that are found in the majority of patients are a low frontal hairline, eyelid ptosis (falling of the upper eyelid), facial asymmetry, and ear deformities. The prevalence is estimated at 1 in 25,000–50,000 live births. The affected population is considered high-risk of developing elevated ICP even after a first operation, requiring a second cranial expansion in the majority of cases [17][16].
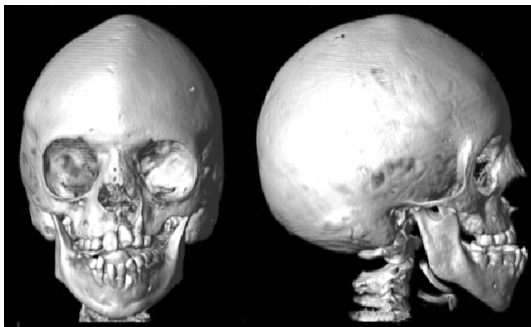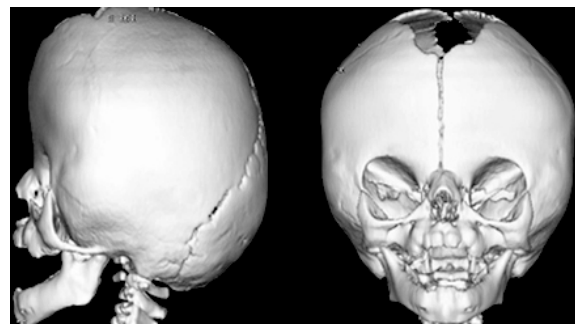

Figure 1.9: Crouzon Syndrome[17]

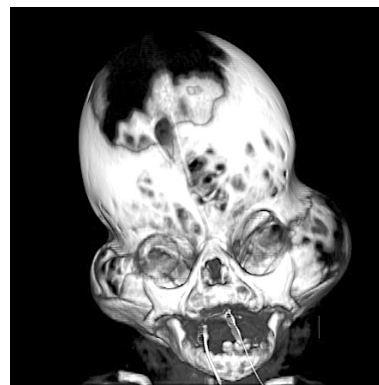Figure 1.10: Apert Syndrome [18]

Figure 1.11: Syndactyly of fingers[18]

Figure 1.12: Cloverleaf skull deformity (Pfeiffer Syndrome) [19]

1.3.3 Consequences of the Craniosynostosis

A healthy brain triples in volume during the first year of life and reaches two thirds of its adult size between the ages of 6 and 10. Skull growth happens thanks to bone apposition (growth by deposition of layers) and the growing brain which causes the displacement of cranial bones. However, this process stops when sutures fuse. This is the most dangerous consequence of craniosynostosis: the inability of the developing skull to accommodate the volume requirements of the growing brain [17]. This leads to skull disproportion and may cause the rise of the ICP. This augmentation of pressure grows exponentially with the number of fused sutures. Other factors are also known for contributing to an increase of the ICP in patients with craniosynostosis: abnormal CSF in circulation, hydrocephalus (accumulation of CSF in the ventricles within the brain) and upper airway obstruction [20].

A delayed diagnosis of elevated ICP may result in optic nerve atrophy, blindness and developmental delay [17]. Intracranial volume, however, is normal for most patients with craniosynostosis. A correlation between the type of craniosynostosis and the different kinds of impairment has been shown: sagittal synostosis seems to be associated with speech and language difficulties as it may alter the occipital and parietal brain as well as the prefrontal cortex. Indeed, those regions are known to be associated with language development and processing of information. Similarly, patients with a metopic synostosis may present some higher neurological function impairments as the frontal lobe, responsible for motivation, planning, social behaviour, and speech production, is distorted [14].

Another frequent consequence of craniosynostosis is the Chiari malformation: it results in the displacement of the cerebellar tonsils down through the foramen magnum. They can obstruct the CSF outflows and cause non-communicating hydrocephalus, leading to headaches, nausea, muscle weakness and even paralysis in the most severe cases [17].

1.3.4 Treatment of Craniosynostosis

There are different ways of treating craniosynostosis; the type and extent of recommended surgery depend on several factors: the age of the patient, the number and location of fused sutures. The surgical team that will perform the procedure generally includes a craniofacial surgeon and a neurosurgeon.

▶ **Endoscopic strip craniectomy followed by helmet therapy**

This surgery is usually recommended for babies younger than 4 months with a single suture fused. During the operation, surgeons use an endoscope; a thin, lighted tube with a camera and small tools attached. This device allows much smaller cuts made to the baby's head and scalp compared to open surgeries. The surgeon can make either small holes in the skull or enters the skull through the softer spots. After separating the skull bone from the protective layer covering the brain (the dura), the surgeon removes the fused suture on the top of the head. They also cut out two small strips of bone on each side of the skull near the ears (Figure 1.13). The patient will then have to wear a specifically fitted helmet for several months following the surgery to mold their head to a shape allowing a normal brain growth. [21]

▶ **Total Calvarial Remodelling (TCR)**

For babies older than 5 months, the reshaping by helmet therapy may be less effective. TCR consists in opening the top of the child's head in a zig-zag pattern (this type of incision makes sure the hair won't part along a straight line scar in the future), removing and reshaping the affected parts of their skull, and then fixing them back in place to create new space (Figure 1.14). [21][22]
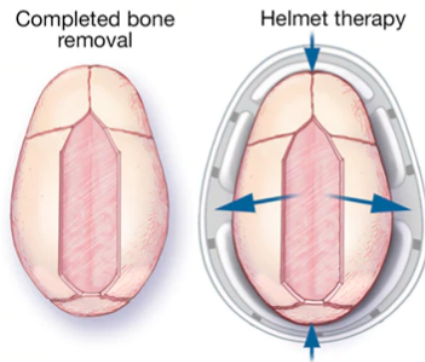

Figure 1.13: Endoscopic strip craniectomy [23]

Figure 1.14: Open remodeling surgery [24]

▶ **Distraction for Fronto-orbital or Posterior Cranial Surgery**

The procedure involves performing controlled cuts in the bones and using a device to gradually separate the bone fragments. Those fragments are then kept apart by the distractors over a period of 1 to 3 months, allowing new bone to form. This process is called distraction osteogenesis 1.4. This type of procedure is usually recommended for babies of any age with a fused coronal suture [25]. For the fronto-orbital case, the reshaping process concentrates on the patient's forehead and the upper part of their eye sockets. After moving this part, creating space for the brain and eyes development, the surgeon fixes it with screws and plates that will be absorbed into the body over time (Figure 1.15) [21]. This technique for posterior vault expansion will be further developed in section 1.4.

▶ **Spring Assisted Cranioplasty (SAC)**

More recently, craniofacial surgeons adopted elastic distractors, such as stainless steel springs, to reshape the skull. This technique is minimally invasive and appears to reduce morbidity and hospital stay [26]. However, potential drawbacks include the need for a second procedure for the springs removal after 4 to 6 months [27] and the lack of published long-term follow-ups [28]. Furthermore, the surgeon currently has very little control over the distance or rate at which bones are separated from one another [17]. In this procedure, the patient is positioned in a sphinx position (facing the table with a cushion to raise the upper body and the head) and depending on the type of craniosynostosis, the surgeon will perform different surgical cuts, used to insert the springs and allow for expansion. The springs are secured in place by means of notches at the desired location (Figure 1.16). This technique will be further developed for the posterior vault expansion in section 1.5.
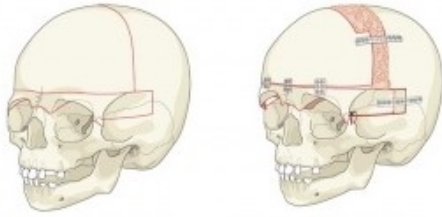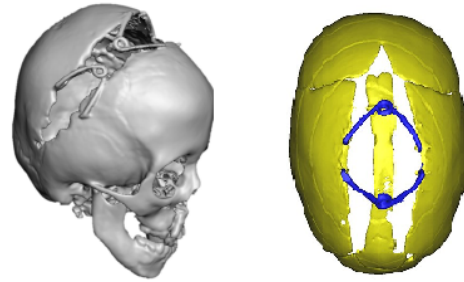
Figure 1.15: Fronto-orbital surgery [29]

Figure 1.16: Spring assisted cranioplasty: coronal (right) [30] and sagittal (left) [31]

1.3.5 Timing for Surgery

The age of the patient at the time of surgery can vary. Most surgeons will prefer to wait until the child is 3 months old to avoid physiologic stresses of surgery, particularly bleeding. However, some surgical techniques like endoscopic surgeries are preferred to be performed as early as possible, even before the 3 months limit as this procedure requires a molding helmet therapy for several months after the surgery. In contrast, helmet therapy is not needed after open surgeries, therefore these operations can be done later. Indeed, the pieces of bone are surgically placed in, and not molded to, the desired position. [14][17]

Nevertheless, the ideal timing for open surgeries is still debated: arguments in favor of early intervention (< 1 year old) are the minimization of cerebral constriction and improved morphological results. Many surgeons consider best to operate between 3 and 6 months of age as during this period, the brain and skull growth is fast and increases the chance for re-ossification and bone re-modeling. However, during this period, cranial bones are very malleable and too weak to support rigid fixations. The bones will become thicker and more rigid after 12 months but this also limits the abilities of reshaping them. In addition, the ability of infant skull to spontaneously repair large bone defects is lost between 9 and 11 months [14][17].

Surgeries can also be performed in the the mid-childhood (4 to 7 years old) to avoid the need of undergoing a secondary surgery in the teenage years.

1.4 Posterior Cranial Distraction

Distraction as we know it has been used to address the fronto-orbital region in craniosynostosis for over a decade; however, its application to the posterior vault (Posterior Vault Distraction - PVD) in syndromic craniosynostosis has been described recently. In this procedure, osteotomies are performed on the calvarium to separate the posterior section and allow for cranial augmentation. The patient is in a prone position, the surgeon will make a bicoronal incision to expose the skull and then perform a posterior craniectomy. Distractors will be fixed on the calvarium and the scalp will then be closed (Figure 1.17). The period of 5 to 7 days following the surgery is called the latency period during which no distraction is applied [25]. After that comes the activation period; the gradual distraction of the osteotomy allows the surgeon unmatched control in gradually increasing the gap between the cranioplasty fragments. The rate of distraction indicates to the number of times the device is activated each day and the rhythm expresses the distance per turning episode that the bone is distracted. These parameters depend on the age but will be generally in the order
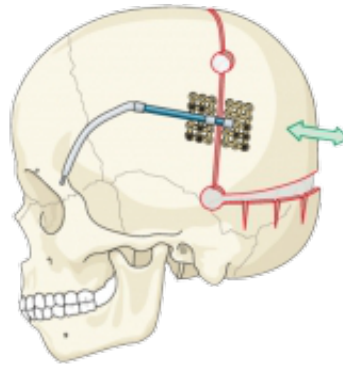
Figure 1.17: Illustration of posterior vault distraction with internal distractors [29].

of half a millimeter to one millimeter by day. The duration of this activation period will therefore depend on the distance estimated by the surgeon and the head shape desired (usually between 20 to 30 days). Finally, after a consolidation period of 6 to 8 weeks with no activation, a procedure is required for the device removal. This time period will help to prevent relapse of the fragments back to their original positions [17]. Many types of distractors are available depending on the manufacturing company and anatomical area targeted. However, they are usually classified in two broad categories: internal and external distractors. Internal distractors are placed beneath the skin with only the turning mechanism sticking out. External distractors are fixed into the bone using pins or screws, but the majority of the device is outside of the body [25]. While the first type is more subtle, it requires a second surgery for the removal; external devices, though, are conspicuous but can be removed in a clinical setting. For this procedure, PVD allows a significant expansion of the intracranial space and improvement in head shape. Indeed, the posterior vault distraction provides a larger volume increase per millimeter of advancement than anterior expansion. This technique also helps patients with the Chiari malformation, thanks to its decompressive effect [17].

1.5   Spring Assisted Posterior Vault Expansion (SAPVE)

The first spring assisted craniofacial procedures were reported by Lauritzen et al. [32] in 1998. The springs were made in the operation room from stainless steel alloys available as wires of different thicknesses. This kind of procedure was then introduced in January 2008 at GOSH after an 8 months period of distractor design for use in scaphocephaly correction.
In case of SAPVE, a preliminary set of CT images is performed to assess the underlying patient anatomy and perform 3D reconstruction of the patient's skull. The timing for these preoperative images can vary according to patients, but usually does not exceed a year before the surgery.
On the operation day, the patient will be put under general anaesthetics, his/her hair will be clipped just over the incision site and fixed out of the way. The surgeons will make an incision from ear to ear, over the top of the head and expose the skull by pulling the skin downwards over the back of the head. Next, they will perform an osteotomy behind the coronal sutures and move the back portion of the skull backwards, leaving a small gap between both parts of the bone. As springs are used to expand the posterior vault, they will be fixed to each side of the cut, into notches provided for this purpose. The number of springs inserted is decided by the operating surgeons in order to give the best shape possible to the skull. As said before, this number usually varies from 2 to 4 but can go up to 6 in some cases. After that, the skin is unfolded back over the

incision and the surgeon will proceed to close it with stitches. One or two drainage tubes will be left in place to collect any leaking fluid and will be removed a couple of days later. The patient will be closely monitored at the hospital during around five days following the operation before being able to go home if his/her recovery is on the right track [26].
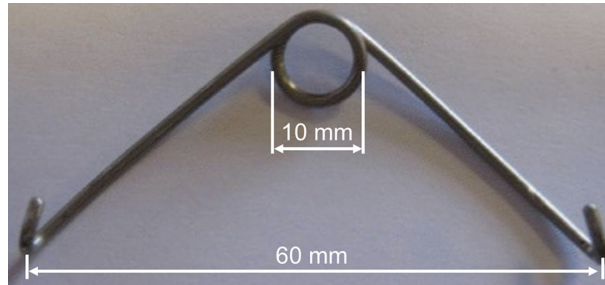

Figure 1.18: Spring model used at GOSH [31].

Although this procedure is usually described as safer than others, a few risks remain. This surgery requires separating the skull bone from the dura, this process can cause brain injury or internal bleeding which could lead to serious complications such as seizures or strokes. However, the overall risk of such major neurological event or death is below one per cent. Spring insertion also carries some specific risks, such as failure or dislodgement of the springs [26].

A series of follow-up appointments will be planned, during which some additional medical images could possibly be recorded. These are useful to track the kinematics of the spring opening or simply verify that they are still correctly in place. Usually, the first postoperative CT scan is done a day or two after the surgery.

The timing of removal differs for each individual child but is usually around six months to a year after insertion. This allows the bone to grow in between the springs, preventing the skull to deform again. Posterior vault expansion has already shown promising results for reducing increased ICP, especially in children with severe craniosynostosis. If pressure rises again later in life, the operation can safely be repeated [26].

1.6 Springs Mechanics

Springs were introduced at the Great Ormond Street Hospital in London, in 2008 for the correction of scaphocephaly in sagittal craniosynostosis performed using spring devices. Those devices are torsional springs made of stainless steel wire with a central loop and an initial opening of 60 mm before implantation (Figure 1.18). These springs exist in three different models (S10, S12, S14) differing by their wire diameters (1.0, 1.2, 1.4 mm respectively) and stiffness (0.17, 0.39, 0.68 N/mm respectively). They follow a Hookean behavior when compressed, meaning that the amount of compression that they underwent is directly proportional to the outwards force they exerted. A mechanical compression test was performed in order to observe the relation between force and opening distance for the different spring models at loading and unloading (Figure 1.19). The compressive force was applied on one tip of the springs placed vertically aiming at reducing the space in between the 2 tips. The initial opening at resting conditions is 60 mm and they are crimped

until an opening of 20 mm is reached and then back to 60 mm again. Springs are equipped with footplates (those footplates will be placed in notches in the skull to secure the spring in place), here they are removed to test more easily (their stiffness is negligible). Thanks to those curves, it is possible to compute the spring stiffness K by measuring the slope of the linear fitting of the curve (Example done for the S12 model on Figure 1.19) [31].
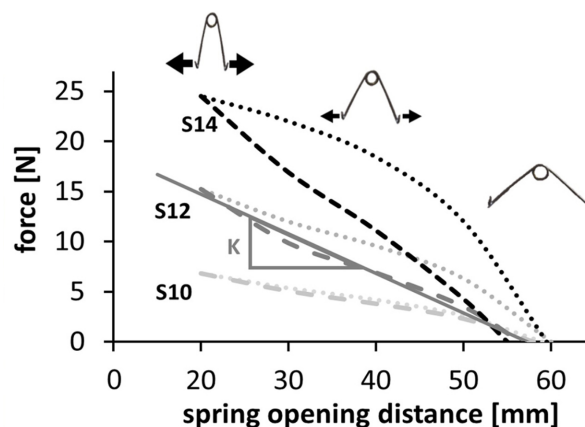

Figure 1.19: Force/opening curve for the different spring models [31].

In a previous study, a group of 60 patients who underwent spring cranioplasty for the treatment of sagittal craniosynostosis was recruited. The surgery average age was 5.2 ± 0.9 months. Each patient was implanted with 2 springs for a duration of about 3 to 4 months [31].

Considering the spring combination per patient, 33 patients received two of the same spring models implanted (S10-S10, S12-S12 or S14-S14). The remaining 27 had a combination of 2 different spring models in the anterior and posterior positions, with no obvious trend for the position of the stiffer spring. One could notice that patients with two S14 models were older (6.0 ± 0.7 months) than those in the other groups (S10-S12: 4.8 ± 1.0 months, S12-12: 5.2 ± 1.0 months and S12-14: 5.2 ± 0.7 months), confirming that older patients generally received stiffer springs [31].

As we know, the stiffness of S10 springs is lower than the others, therefore, the force exerted at insertion and at the first follow-up is also lower than the force for S12 and S14 (same thing for S12 compared to S14). If insertion was day zero, the time of the first follow-up (FU1) was around 1–2 days for 60 patients, whereas the second follow-up (FU2) happened after 6 to 59 days (mean: 22 days) for 57 patients [31].
The combined opening and force plots over time showed the progressive spring opening from insertion to removal, while spring forces decayed, with a statistical difference in opening and force between each consecutive time point (Figure 1.21 and Table 1.20).

| Time | Combined Opening (mm) | | Combined Force (N) | |
Point	Mean ± SD	p Value	Mean ± SD	p Value
Insertion	30.1 ± 4.3	0.002	23.7 ± 8.6	<0.001
FU1	43.7 ± 6.0	0.03	10.3 ± 4.7	0.001
FU2	53.1 ± 3.8	0.01	2.5 ± 3.3	NS
Removal	55.0 ± 2.6	NS	1.6 ± 2.4	NS

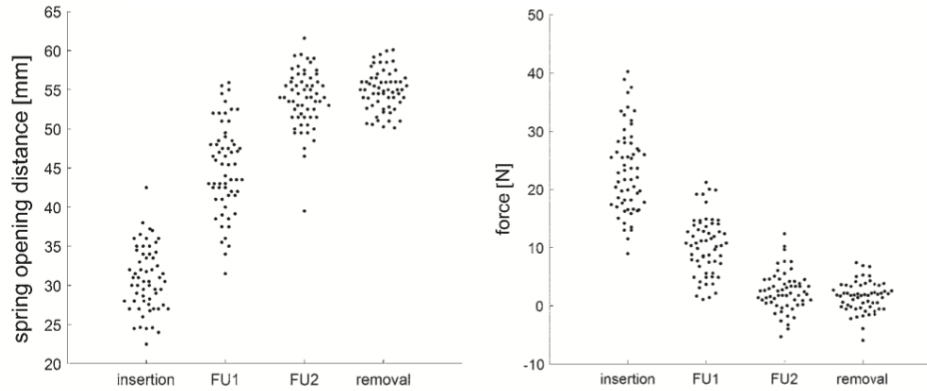Figure 1.20: Spring opening distance and force values at different time points [31].

Figure 1.21: Combined spring opening distance (left) and force (right) at insertion, FU1, FU2 and removal [31]

1.6.1   Springs Kinematics

The spring kinematics was studied using the opening values at the 4 time points, from insertion to removal. It was assumed that the skull behaved as a viscoelastic material and that the spring opening distances followed an exponential curve governed by a time constant τ [31]:

$$OP(t) = OP_{IO} + (OP_{RO} - OP_{IO}).(1 - e^{-\frac{t}{\tau}}) \qquad (1.1)$$

Where, OP_{IO} is the opening at insertion and OP_{RO}, the opening at removal.
In an exponential rise, τ represents the time at which the analyzed data reaches $(1 - 1/e) = 67\%$ of its maximum value. Here, τ is therefore, the necessary time for the springs to reach 67% of its maximum opening i.e. 60 mm. The model fitting was carried out using the nonlinear least squares method, implemented in MATLAB (MathWorks). This time relaxation value was computed for each patient and the normal probability distribution of the data was tested to obtain the average and standard deviation of τ in the population [31].

To assess the timing of the springs kinematics, two properties of exponential rise have been taken in account:

1. The exponential function reaches its plateau after 5τ

2. In a normal distribution (mean, μ and standard deviation, σ), Chebychev's inequality states that 97.8% of the population is found within the interval $[-\infty, \mu + 2\sigma]$.

Knowing that, it can be conclude that 97.8% of spring will reach the opening plateau after a time:
$T = 5(\mu_\tau + 2\sigma_\tau)$.

After the model fitting for patients with sagittal craniosynostosis, the value of τ retrieved was
about 1.16 ± 0.46 days meaning that the springs were extended at 67% of their maximal opening
after a little more than 1 day. Therefore, the population time T was calculated as 10 days (for
98.7% of the springs to reach the opening plateau).
Figure 1.22 depicts the comparison between the spring opening distance at 10 days (OP_T) and the
opening distance measured on the operating table at removal (OP_R), showing a good correlation
and an absolute difference of 0.06%$\pm$ 0.17% [31].
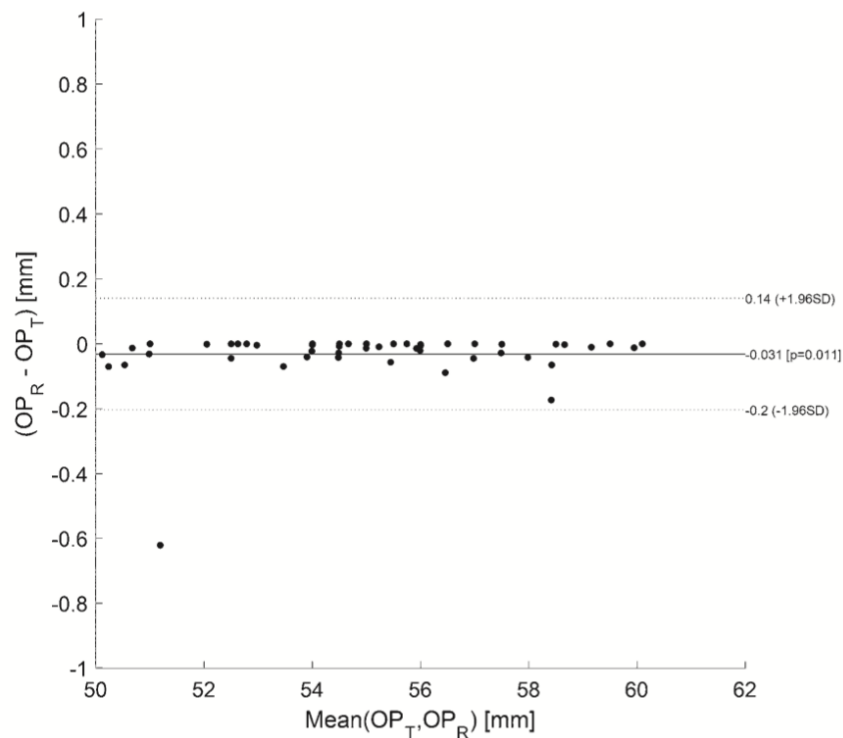
Figure 1.22: Bland-Altman plot of the comparison between the spring opening at removal (OP_R)
and the opening at 10 days (OP_T) [31].

1.7 Prediction of SAC: Finite Element Analysis

1.7.1 Aim of Finite Element Modelling for SAC

A number of studies have already been conducted on the correction of scaphocephaly caused by
the fusion of the sagittal suture. Like this project, those studies aim to predict the resulting head
shape based on a patient-specific computational model. The final goal is to use this technique to
perform prospective prediction of springs dynamics to inform surgical planning, distractor selection
and improve preoperative patient information [33].

1.7.2 Segmentation From CT Scans

The preoperative CT scans retrieved for each patient were segmented in `Simpleware` to isolate the skull from soft tissues and to be prepared for the simulations.

In the work by Breakey et al. [34], a population growth curve was created based on the bone surface of 24 unoperated sagittal craniosynostosis patients (age at CT scan: 4.0 ± 1.3 months). This curve was used to rescale the CAD models in order to take the growth in between the preoperative CT and the surgery into consideration [33].

The next step consists in making the osteotomies in `Simpleware` based on the real measurements recorded in theatre during surgery. In case of sagittal craniosynostosis correction, two osteotomies are made parallel to the fused suture at a distance LAT extending from the coronal to the lambdoid sutures. Then the craniectomy of squared piece of bone is performed in order to insert the springs, one anteriorly and one posteriorly (Figure 1.23).

All models are meshed identically using tetrahedral elements in `Simpleware`; the mesh density was selected depending on the convergence of the simulated spring extension and the computation time [33].
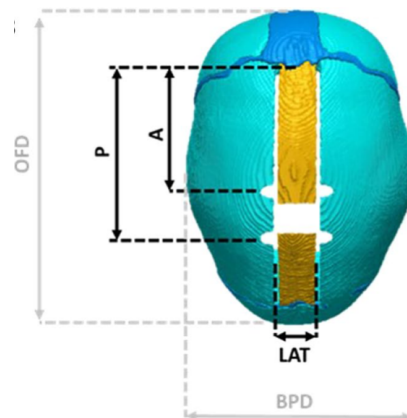

Figure 1.23: Osteotomies and measurements recorded during surgery: A = distance between the coronal suture and the anterior spring; P = distance between the coronal suture and the posterior spring; LAT = dimension of the parasagittal osteotomy; OFD = occipitofrontal diameter; BPD = biparietal diameter [33]

1.7.3 Importing in `Ansys`

The skull geometry was then imported in `Ansys Mechanical 17.2` as an external model linked to a static structural analysis system.

The base of the model was fully constrained to mimic the presence of the calvarial skull base. The springs were then inserted using the linear conditions implemented in `Ansys` to simulated the effect of implantation [33]. Data of bone and suture elastic and viscoelastic properties were initially retrieved from literature [35][36].

1.7.4 Results of the Simulations

In case of sagittal craniosynostosis correction, the simulations were performed to observe the complete spring expansion over 10 days (Figure 1.24). Results have shown great shape matching

between the simulated head shape and the CT scans. In the work of Borghi et al. [33], the comparison was made in terms of surface distance patterns and surface error distribution. It has been demonstrated that, for the population of the study, 80% of the error was below 2 mm. The model also managed to estimate the cranial index with a discrepancy of less than 2%.
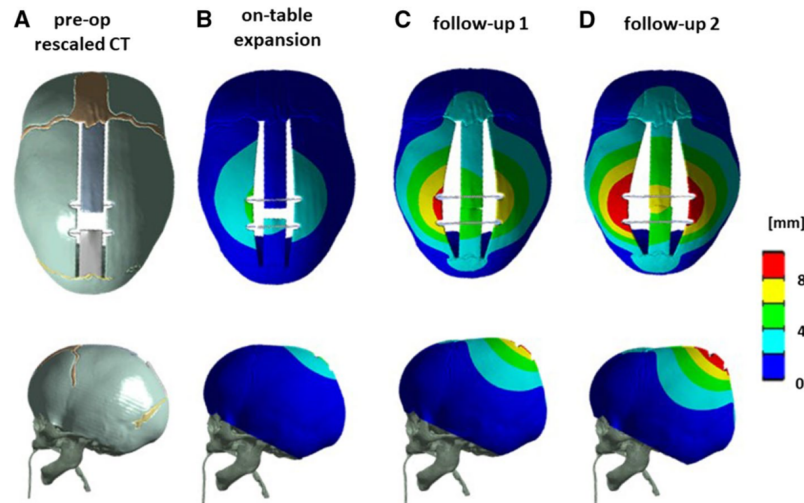

Figure 1.24: **a** Preoperative model with spring inserted, **b** simulated expansion on-table, **c** at follow-up 1, and **d** follow-up 2 for a representative patient [33].

1.8   Main Aims of the Thesis

The main goal of this thesis is to model the posterior vault expansion using finite element simulations. Those patient-specific models will be created based on preoperative computed tomography images. Currently, the PVE surgeries are performed according to the operating surgeon's experience and the dimension and position of osteotomies (bone cuts) are selected on-table as well as the type, position and number of springs to be inserted. This method has led to complications and revision rates of over 10% in GOSH centre since 2008. Therefore, the final objective is to develop a three-dimensional finite element simulation platform that will be used by surgeons performing spring-assisted PVE procedures as a preoperative planning tool as well as a teaching and learning aid.

Chapter 2

Materials and Method

2.1 Patient Selection

The population of this project was selected among the GOSH patients database who underwent a SAPVE, affected by Apert, Crouzon, Pfeiffer or Multi-sutural (no specific genetic diagnosis) syndrome. The selection of the 14 patients was based on the availability of both pre- and postoperative CT scans for each patient and the presence of visible springs in the postoperative reconstructions. The Table 2.1 below shows the list of patients recruited and their personal details.

Patients	Age surg. (Days)	Time (Days)		Syndrome	a
		Preop CT-Surg	Surg-Postop CT		
P1	193	55	162	Apert	239.1
P2	234	3	67	Cranial Dysraphism	157.9
P3	237	47	29	Apert	239.1
P4	299	66	70	Multi-sutural	157.9
P5	381	49	112	Crouzon	148.5
P6	393	4	57	Apert	239.1
P7	464	1	6	Pfeiffer	148.5
P8	479	232	266	Multi-sutural	157.9
P9	523	16	562	Crouzon	148.5
P10	533	14	280	Crouzon	148.5
P11	1075	32	144	Crouzon	148.5
P12	1534	8	152	Multi-sutural	157.9
P13	1992	10	86	Multi-sutural	157.9
P14	2044	74	68	Multi-sutural	157.9

Table 2.1: Patients' details constituting the population of this project

2.2   Pre-processing

2.2.1   Segmentation

In computer vision, image segmentation is the process of partitioning a digital image into multiple segments (set of pixels). Medical image segmentation is the process of automatic or semi-automatic detection of boundaries within a 2D or 3D image in view of assigning a label to every pixel of the image so that pixels with the same label share certain characteristics. The goal of segmentation is to simplify and/or change the representation of an image into something that is more meaningful and easier to analyze [37].

The simplest method of image segmentation is called the thresholding method and is the one used in this project. This method is based on a threshold value interval to turn a gray-scale image into a binary image. The key of this method is to select those threshold values and this is what this section will be describing [38].

Starting by importing the DICOM files, corresponding to the raw CT scan data, into `Simpleware ScanIP`, the bone needs to be differentiated from the rest of the tissues to isolate the region of interest, which is the skull.

At this stage, in order to get a better visual representation, a volume rendering preset can be added to highlight a particular region. However, in our case this is not necessary as the skeleton is easily discernible from the other parts of the scan (Figure 2.1).
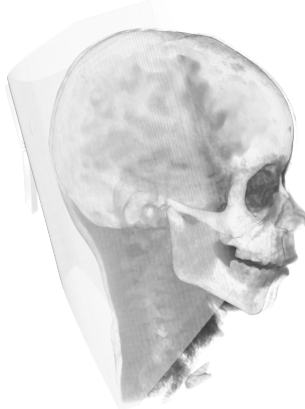
Figure 2.1: Raw CT-scan data viewed in `Simpleware`.

Then, as explained above, the soft tissues have to be removed by defining a threshold interval in order to segment the skull away from the rest of the image.

After creating a new mask, the values of the density threshold have to be determined to carry on the segmentation. To identify which range of values to use, the software offers a *profile line collaboration* tool. The latter shows the density grey-scale values on a profile line on a chosen study slice. Once a clear slice has been selected, a line is drawn across a region that we know is bone (Figure 2.4). This will give the changes in density along that line and enable us to find the density interval of bone to enter in the threshold tool (Figure 2.2). This results in the isolation of all pixels contained within this interval. As can be seen on Figure 2.3, this includes the panel around the child's head and a part of his spine which are not needed for our application.

To clean the model and obtain only the skull part of the scan, the *Flood Fill* tool will be used to create one continuous model. By clicking on a pixel from the cranium, we are able to isolate it from the rest (Figures 2.5). Sometimes it can happen that the top of the spine remains after this operation; in this case, the *Unpaint* tool would be used to dissociate it from the skull and perform *Flood fill* once again. The result for all 14 patients are depicted further in the report on the left side of Tables 2.3 to 2.6.
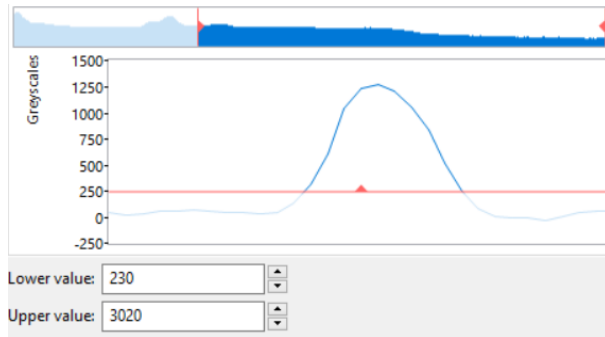
Figure 2.2: Profile line resulting from the selection in Figure 2.4.

Figure 2.3: 3D result of threshold tool.

Figure 2.4: Selection of a bony area to determine the threshold values.
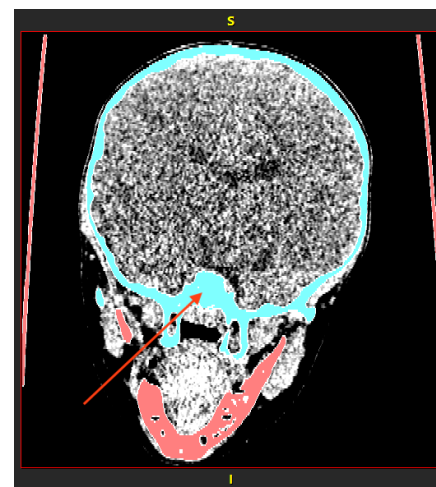
Figure 2.5: Pixel selection to use the *Flood Fill* tool on the blue region.

2.2.2   Volume Scaling

To compare the simulated model to the postoperative CTs, the time period and underlying growth between the surgery and the preoperative CTs images have to be taken into account. That is why the model created from the preoperative CT has to be re-scaled considering this time to enable a relevant comparison.

Breakey et al. published a study [34] on analyzing intracranial volume gain and tracking head circumference growth in children with unoperated syndromic craniosynostosis. The goal of this

work was to provide syndrome-specific reference growth curves to enable the monitoring of intracranial volume over time to allow comparison.

The scans retrieved for this study had to meet certain criteria: to have a slice thickness inferior to 3 mm and to include the full region between the vertex and the foramen magnum.
After that, the ICV was calculated automatically using `FSL` (FMRIB Analysis Group, Oxford, United Kingdom) and a semi-automatic approach using `Simpleware ScanIP` if the first technique failed to extract the entire cranial vault.

The population of this work counted 229 syndromic patients. One hundred forty- seven of them had 243 CT scans before any surgery was carried out. Two hundred twenty-one of those CT scans remained eligible for the study (93 Apert scans, 117 Crouzon-Pfeiffer scans and 33 Saethre-Chotzen scans). The mean age across all syndromic groups was 2.4 years (range: 1 day to 17.5 years) and for the control group, the mean age was 5.4 years (range: 6 days to 15.7 years).

The growth curves resulting from this study are displayed in Figure 2.6.

Therefore, to re-scale the volume of the patient's head before performing the simulations, we are going to base our calculations on the curves of unoperated syndromic children.
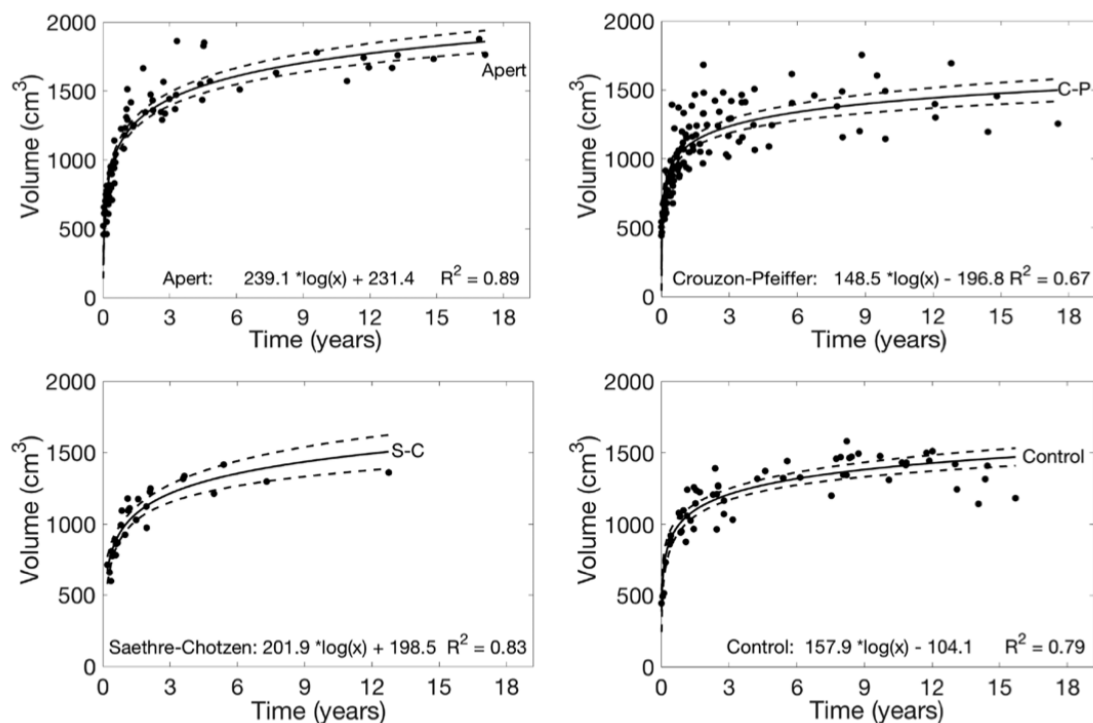
Figure 2.6: Intracranial volume growth curves showing (top left) Apert syndrome patients, (top right) Crouzon-Pfeiffer syndrome patients, (bottom left) Saethre-Chotzen syndrome patients, and (bottom right) control patients. Solid line represents the fitted logarithmic curve; dashed lines represent 95% confidence interval. The equations provide the volume in cube centimeters when given age(x) in days [34].

The Table 2.1 in Section 2.1 lists the patients details used in this project. In some cases the pre-operative CT was retrieved months before the surgery. Knowing the patient's age on the operation day and the time in between surgery and the acquisition of the first CT, the age at CT can easily be calculated. These values will be used to compute the multiplication factor which will multiply the pre-operative volume from the first CT in order to obtain a good approximation of the volume on the surgery day.

The preoperative ICV values were retrieved from the previously introduced study of Breakey et al. [34] since our patient selection is part of its population.
Using the logarithmic curves from that same study, we are able to select the parameter defining the logarithmic growth, a, according to the patient's syndrome (Figure 2.6, Table 2.1). The equation for ICV calculation in Apert's patients is shown in Figure 2.6 (top left) and can be broken down as follows:

$$ICV = a \times \log(x) + b, \tag{2.1}$$

Where x is the age in days and b the base value for the specific syndrome.

To recalculate the ICV at the time of the surgery, b must be first adjusted to the patient specific value using the ICV of the pre-operative CT and the age at the CT acquisition (age_{CT}):

$$b_{adjusted} = ICV_{CT} - a \times \log(age_{CT}) \tag{2.2}$$

The ICV on the day of the surgery (ICV_{surg}) is then obtained using the adjusted value $b_{adjusted}$, and the age of the patient on the day the springs were inserted (age_{surg}). The equation 2.1 therefore becomes:

$$ICV_{surg} = b_{adjusted} + a \times \log(age_{surg}) \tag{2.3}$$

Finally, the multiplication factor is obtained by:

$$\text{Multiplication factor} = \left(\frac{ICV_{surg}}{ICV_{CT}}\right)^{\frac{1}{3}} \tag{2.4}$$

The volume growths resulting from these calculation were on average in the range of $[0.006; 3.5]\%$. All volumes and factors computed are presented in Table 2.2.

The *Rescale* tool in `Simpleware` allows to enter the percent of change in all directions, i.e. the multiplication factor.

Patient	v_{pre} (cm^3)	v_{surg} (cm^3)	Multiplication factor
P1	1081.82	1162.02	1.024124
P2	896.07	898.11	1.000757
P3	974.96	1027.81	1.017752
P4	1538.92	1578.30	1.008458
P5	1245.01	1265.45	1.005444
P6	1583.09	1585.54	1.000515
P7	1735.54	1735.86	1.000062
P8	953.54	1058.12	1.035298
P9	1268.56	1273.17	1.001211
P10	1105.72	1109.67	1.001190
P11	1264.21	1268.7	1.001182
P12	1566.94	1567.77	1.000176
P13	1686.13	1686.92	1.000157
P14	1330.4	1336.22	1.001457

Table 2.2: Preoperative volumes on the CT and surgery days, and multiplication factor for each patient.

2.2.3   Replication of the Surgical Cuts

Once the model was scaled, the osteotomies (surgical cuts) had to be replicated. To that purpose, a new mask was created in `Simpleware` by extracting the surface of the postoperative CT: the latter had to heretofore be meticulously aligned with the preoperative scan in `Meshmixer`.

This alignment would allow the replication of the osteotomies on our model in concordance with the real surgical cuts from the postoperative reconstruction. Those cuts can be of different shapes (straight, L-shaped or more complex) depending on the final outcome desired. To be consistent with each model, the width of the osteotomies was fixed at a scale of 1 and the length of the notches created at the springs locations was fixed at a scale of 5 with the same width. All these operations had been made using the *3D editing* tool. To finalise the preparation of the model, a few more tools such as *Smoothing filters, cavity fill* and *island removal* were used to removed minor imperfections and cavities in order to simplify the surface of the model.
To reduce the computation time as much as possible in the simulation part, a plane cut was made for each model in the aim of removing complex elements that were not relevant for our analysis such as the nose, teeth and mandible. However, the cut had to be made carefully so that the base of the skull and the foramen magnum were preserved for the future intracranial volume evaluation. In certain cases, the fontanelles and/or bigger defects had been closed, still aiming at simplifying the model for the simulations.

By dragging the updated mask into the *FE model* tab, a new finite element model was created. The model configuration options could then be modified as desired; to generate a model dedicated to the import in `Ansys`, the export type was set to *Ansys workbench volume (solid/shells)(legacy)*. In the *volume meshing* tab, the coarseness of the mesh (ranging from -50 to 0 which represents a coarser to finer mesh) was chosen as well as the order of the elements; the software offered the

choice between 2 orders: linear and quadratic.

A linear element or first order element will have nodes only at its corners while a second order element or quadratic element will have mid side nodes in addition to nodes at the corner.

In the *Node sets* tab, the different node sets destined to apply the boundary conditions were determined. Two options were considered and will be developed in a further section.

Once the model was setup, the full FE model was generated and exported in a *.cdb* files.

The results obtained after simplifications and the creation of the surgical cuts are compared to the preoperative 3D reconstruction just after the segmentation in Tables 2.3 to 2.6.
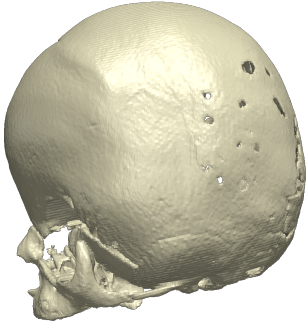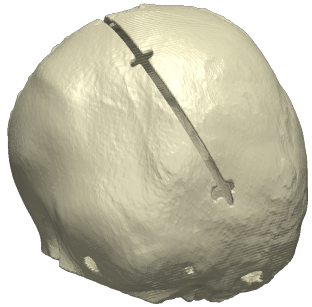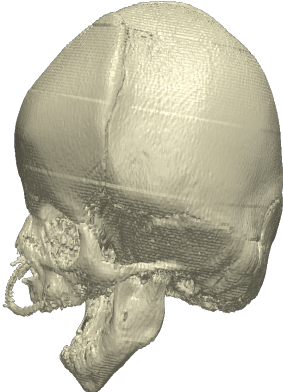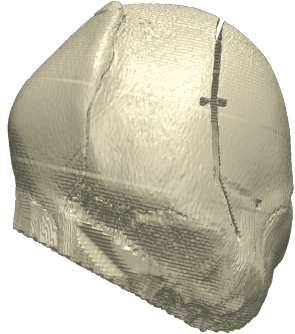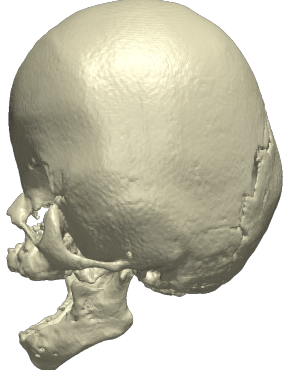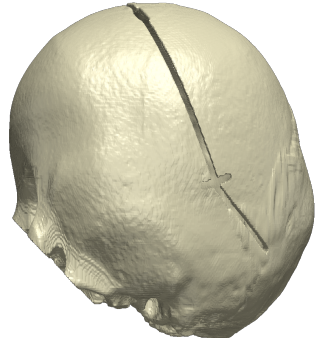
Patient's information	Preoperative CT after segmentation	Model ready for exportation
Patient 1 Age at surg.: 6 months Apert		
Patient 2 Age at surg.: 8 months Cranial Dysraphism		
Patient 3 Age at surg.: 8 months Apert		

Table 2.3: Illustrations of the 3D models after the surgical cuts and simplifications
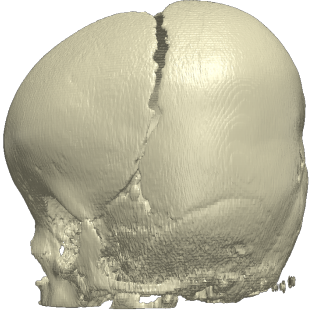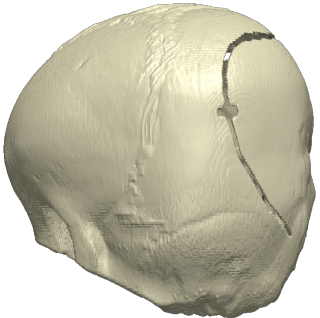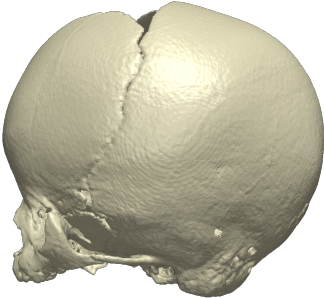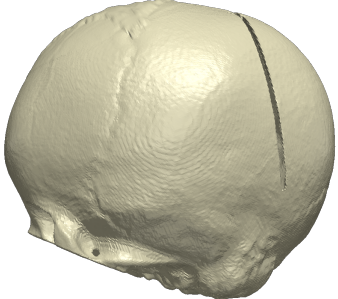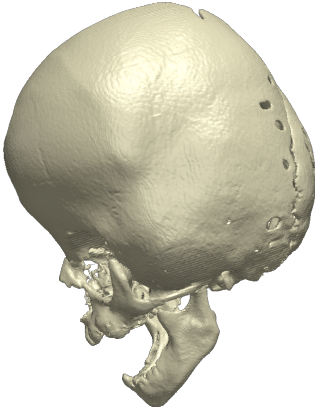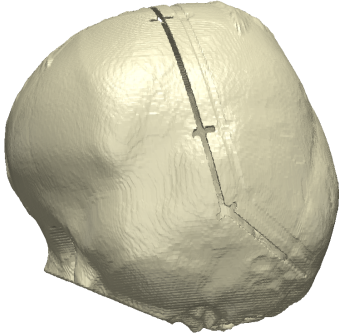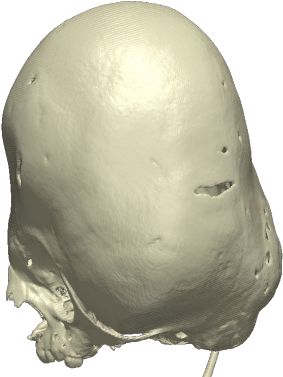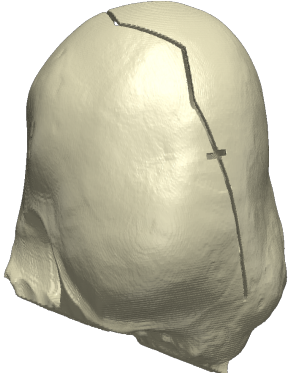
Patient's information	Preoperative CT after segmentation	Model ready for exportation
Patient 4 Age at surg.: 10 months Multi-sutural		
Patient 5 Age at surg.: 13 months Crouzon		
Patient 6 Age at surg.: 13 months Apert		
Patient 7 Age at surg.: 15 months Pfeiffer		

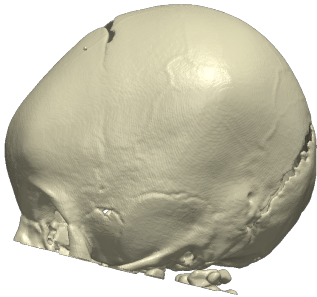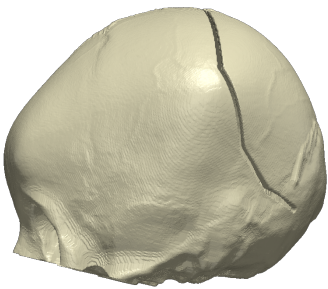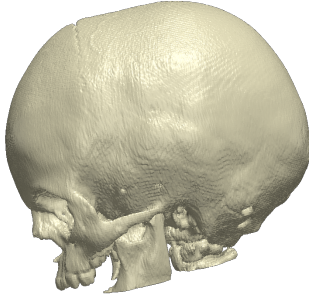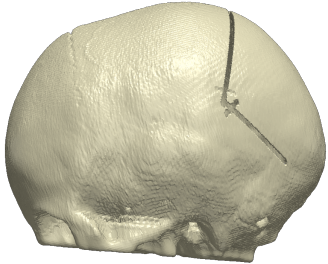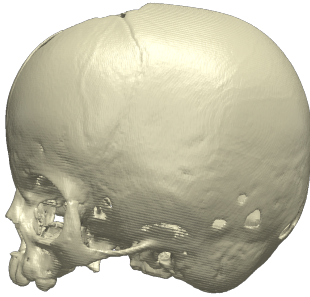Table 2.4: Illustrations of the 3D models after the surgical cuts and simplifications (continued)
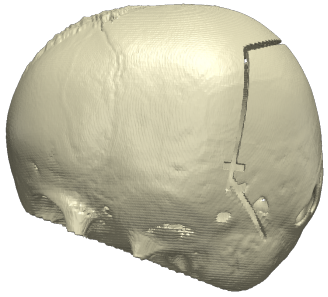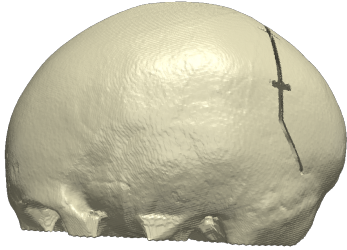
Patient's information	Preoperative CT after segmentation	Model ready for exportation
Patient 8 Age at surg.: 16 months Multi-sutural		
Patient 9 Age at surg.: 17 months Crouzon		
Patient 10 Age at surg.: 18 months Crouzon		
Patient 11 Age at surg.: 2.9 years Crouzon		

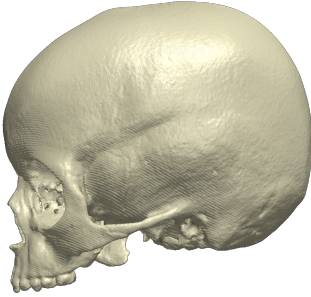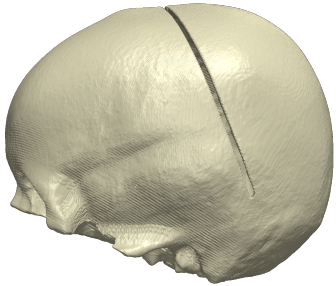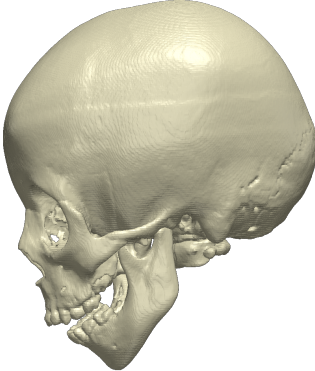Table 2.5: Illustrations of the 3D models after the surgical cuts and simplifications (continued)

Patient's information	Preoperative CT after segmentation	Model ready for exportation
Patient 12 Age at surg.: 4.3 years Multi-sutural		
Patient 13 Age at surg.: 5.5 years Multi-sutural		
Patient 14 Age at surg.: 5.7 years Multi-sutural		

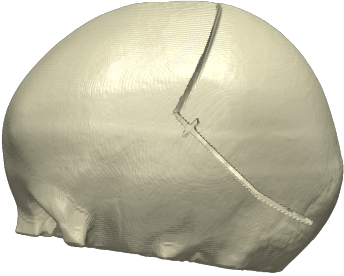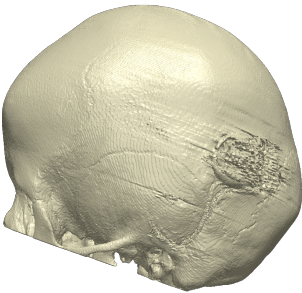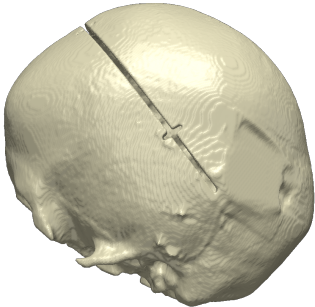Table 2.6: Illustrations of the 3D models after the surgical cuts and simplifications (continued)

2.2.4 Importing in Ansys Workbench 19 R1

In Ansys workbench, a static structural analysis system was created and an external model was added as well. The *.cdb* files obtained previously was imported in this external model and the units had to be checked to make sure the model was imported at the right scale i.e. millimeters. This external model will be used as geometry for the simulations, both systems can therefore be linked together.

2.2.5 Set up in Ansys Mechanical

Since the models had already been automatically meshed in Simpleware, all that was left to do was: define and place the springs and the boundary conditions.

For that, we began by adding *Connections* i.e. springs to the model. Each spring extremity (anterior and posterior) had to be defined using a *Named Selection* beforehand. Depending on the type of springs needed, the stiffness and the preload i.e. free length, were defined. Three different

types of springs are used in GOSH; their mechanical properties are included in Table 2.7 and retrieved from the literature [31]. The reference and mobile body are represented by the anterior and posterior part of the skull respectively. Therefore each side of the spring was applied by *direct attachment*.

Spring Model	Longitudinal Stiffness (N/mm)	Free length (mm)
S10	0.17	60.7
S12	0.39	57.3
S14	0.68	55.6

Table 2.7: Spring mechanical properties

In the *Static Structural* ribbon, the nodal displacement at the boundary conditions, defined as a named selection as well, was fixed in every directions to avoid rigid displacements.
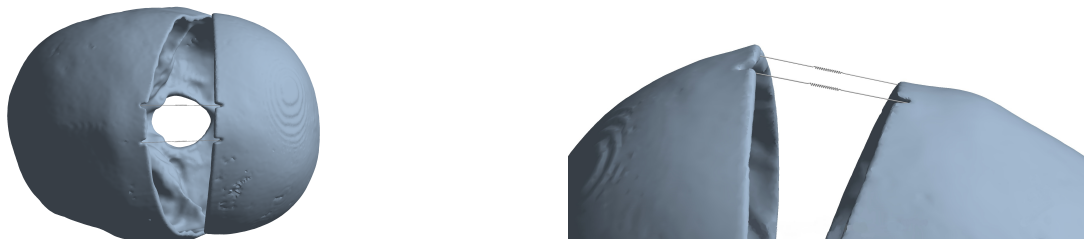

Figure 2.7: Top and side view of the springs insertion in Patient 12

2.2.6   Choice of the Mesh: Mesh Dependency Analysis

To determine the optimal meshing for our models, several size of elements were tested in a mesh dependency analysis. For 5 patients (four of them with 2 springs and one with 4 springs), 10 different meshes were analysed. Two factors were taken into account: the order and the size of the elements. As reported above, `Simpleware` allows the choice of the mesh coarseness in a the range -50 to 0 which represents the evolution from a coarser to finer mesh (i.e. the number of elements increases) and the choice between linear or quadratic elements.

Several graphs were grouped to represent the evolution of the total deformation in function of the number of elements and their order.

As can be observed in Figure 2.9, the cases with quadratic elements seems to converge faster, and to overall a larger deformation, than the linear ones. Simulations were solved for the 10 cases and helped in making the decision of which mesh to keep for the rest of the project, the choice was based on accuracy and time performance. At first glance, quadratic elements seem to be the best choice as the deformation doesn't vary too much with the number of elements. However, when the model was simulated after spring insertion, the simulated model appeared to be deformed in an unrealistic way leading to larger deformation values (Figure 2.8). That problem did not occur with linear elements. As a result, the following parts of the project will consider first order elements.

Figure 2.8: Comparison between simulations with linear elements (left) and quadratic elements (right) for patient 3.

Then came the choice of the appropriate coarseness. Only a few millimetres of difference were observed between the coarseness -30 and -10, however the finer mesh took a large amount of CPU time to solve (10 ± 2 hours). That's why, to achieve a trade-off between accuracy and computation time, the -20 coarseness was chosen and the efficiency of the model will be depicted in a further section.
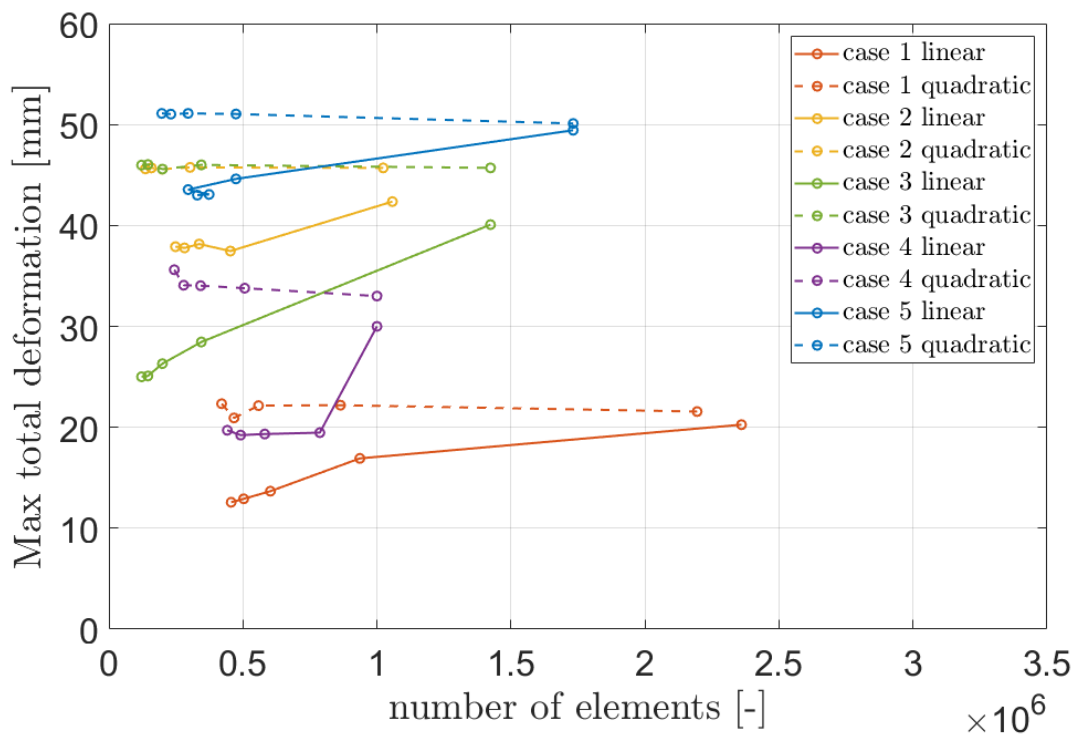

Figure 2.9: Evolution of the total deformation in function of the number and order of the elements

2.2.7   Choice of Boundary Conditions

A set of boundary conditions had also to be determined. These conditions represent which parts of the skull were fixed in all directions during the simulations. Two possibilities were explored: the

entire skull base and the Foramen magnum only (Figures 2.11). Both had been tested by Nagasao and al., 2011 [39].

It is visible in the Figure 2.10, that the difference does not exceed 4 mm for the most extreme case (these data correspond to the deformation of linear elements of coarseness -30 and -20). This slight difference was considered negligible, especially for the finest mesh. Constraining the foramen magnum was considered a better option since it allowed better consistency throughout the patient population.
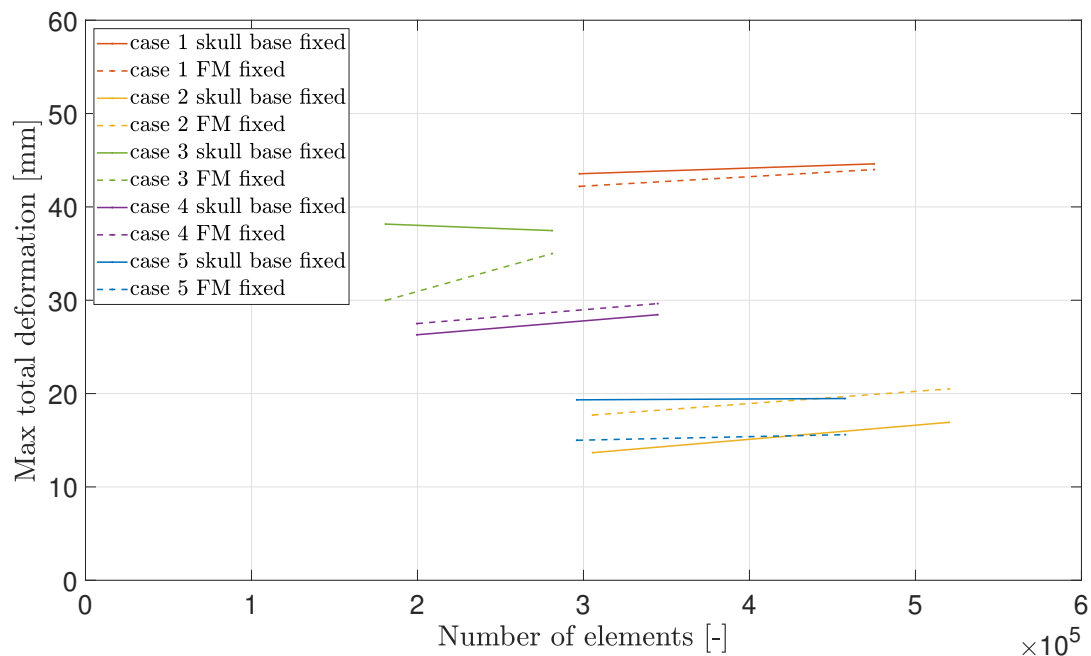

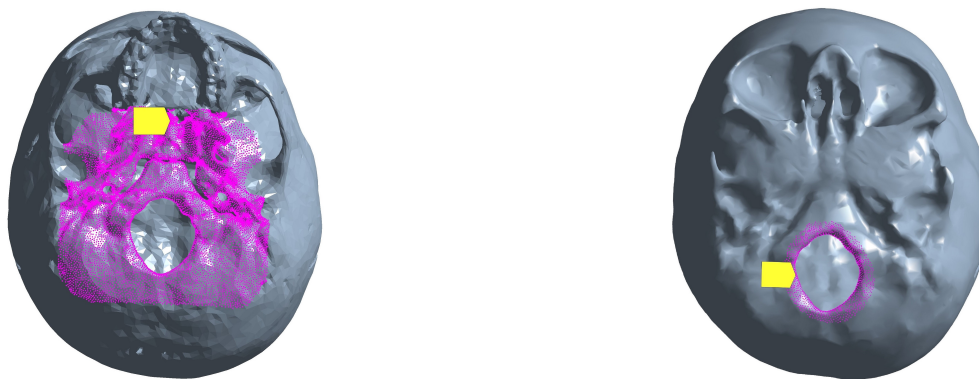Figure 2.10: Evolution of the total deformation in function of the boundary conditions

Figure 2.11: Boundary conditions : Skull base fixed (Right) and Foramen magnum fixed (Left).

2.2.8   Material Assignment

The mechanical properties of bone for the first batch of simulations were taken from a previous work on FE modelling of sagittal craniosynostosis correction [35].

A new material had thus to be defined in the engineering data in `Ansys`: The calvarium was considered as a viscoelastic material with Young's Modulus of $E = 1300$ MPa and Poisson's ratio of $n = 0.22$ [35][36].

Young's Modulus	Poisson's ratio	Bulk modulus	Shear modulus
1300 MPa	0.22	773.81 MPa	532.79 MPa

Table 2.8: Elastic material properties of the skull

In mechanical solutions from `Ansys`, the viscoelastic behavior of the skull material is implemented through the use of Prony series. The shear modulus G, the Young's modulus E and the Poisson's ration ν are related by Eq.2.2.8 for isotropic and homogeneous materials:

$$G = \frac{E}{2(1 + \nu)}$$

Instead of G being constant, it is represented by Prony series in viscoelasticity [40]:

$$G(t) = G_0 \left[\alpha_\infty^G + \sum \alpha_i^G e^{-\frac{t}{\tau_i}} \right]$$

This equation mean that the shear modulus is represented by a decaying function of time t. Therefore, we need to provide pairs of relative moduli α_i and relaxation time τ_i, which represent the amount of stiffness lost at a given rate.

In our case, the material properties were first retrieved from literature [36] and optimized in the work of Borghi et al. [33] resulting in the constants in Table 2.9.

Index i	Relative moduli (i)	Relaxation time (i) [s]
i=1	0.73213	6720.4
i=2	0.25208	40322

Table 2.9: Viscoelasticity properties.

Chapter 3

Result Analysis

3.1 Simulations

A curve fitting was done for patients with sagittal craniosynostosis [31] and the value of τ retrieved was about 1.16 ± 0.46 days meaning that the springs were extended at 67% of their maximal opening after a little more than 1 day [33]. Therefore, the population time T was calculated as 10 days. A simulation over 10 days was run for the fourteen 3D models and the results of total deformation were then exported as *.stl* file (Figure 3.1). These files were then aligned in `Meshmixer` to compare the simulated end-of-expansion with the actual postoperative CT scan. The results of these comparisons are depicted in Tables 3.2 to 3.5 below. However, in order to better observe the physical expansion, The Appendices contain a figure for each patient regrouping the comparison with the preoperative CT as well.
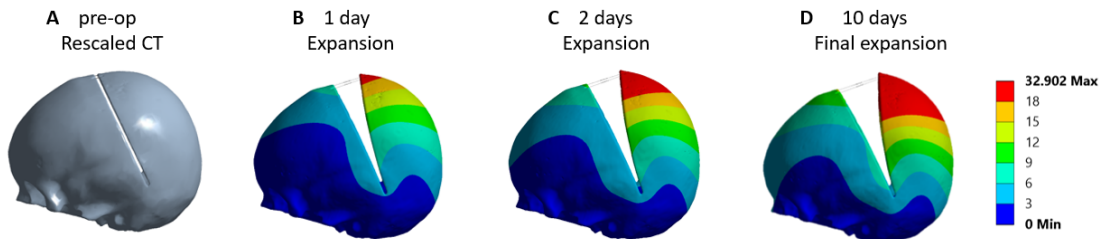

Figure 3.1: **a** Pre-operative model with osteotomy and spring conditions, **b,c,d** simulated spring expansion over time for a representative patient.

From those tables, one can notice that, for the most part, the simulated model closely matches the postoperative CT scan. However, for a few patients (8, 9, 11, 13) it must be noted that the upper part of the occipital bone was cut during surgery to improve the final shape.
The case of Patient 7 required further attention: the total simulation time was set to 6 days instead of 10 as the patient had his postoperative scan 6 days after the surgery and one can observe that the two reconstructions don't match. Such observation hints that relaxation properties for the calvarium of patients affected by syndromic craniosynostosis are different from those of the published population (patients affected by sagittal craniosynostosis). This result suggests that the relaxation time is longer for the considered population. For this reason, the spring kinematics will be studied in a further section for the specific cases of patients who underwent a posterior vault expansion procedure.

3.2   Intracranial Volumes

The prediction accuracy of the model was then tested in terms of ICV calculated in `Meshmixer`. First, the *.stl* files of the expanded model was exported from `Ansys`, it must be ensured that the model is in true scale to have the correct expansion. This file was then imported in `Meshmixer` and re-scaled as `Ansys` usually exports files in meters. To do that, we used the *Transformation* tool and set the scale in every directions to 1000. Using the *Selection* tool, all cut and defect contours were selected and deleted; the aim being to completely dissociate the inner and outer shells of the skull (Figure 3.2).

After using the *Separate Shell* tool, only the inner one was kept and all the small islands remaining from the previous step were cleaned out. It could be noticed that the model was composed of two colors: grey and stripped with light pink. These colors delimit the active work surface (grey) and the inactive one (pink). At this stage, the active surface was defined as the inside of the inner shell (Figure 3.2 (left)). To invert it, the entire shell was selected and we used the *Flip Normal* tool located in the *Edit* tab.

Once this was done, the *Fill* and *Bridge* tools would be used to close the holes and the osteotomy of the model.

Finally, the Figure 3.3 illustrates the final shape: its volume was calculated by the software with the *Stability* tool in the *Analysis* tab. The volume obtained is basically equal to the volume of the brain and can be compared to the ICV from the postoperative CT, computed in a previous study [30].

Figure 3.2: Outer shell of the skull once the defect contours have been removed (Left) and inner shell of the skull (Right).

Figure 3.3: Front and side views of the final intracranial volume to evaluate.

The comparison of all the ICVs calculated in `Meshmixer` are depicted in a bar chart (Figure 3.4). Once again, it is clear that the simulation of Patient 7 is not correctly estimated with a volume difference of about 479 cm³. In addition, we also noticed that the younger patients in

general have greater differences; the latter could be explained by the fact that, for young patients, most of the other sutures are still opened and could therefore move differently. For our models, most of the sutures and defects were closed to simplify the meshing process and optimize the computation time during the simulations but it is something to keep in mind. Usually, it appeared that with all the fontanelles and other sutures opened, the entire cranium would be slightly wider. However, these parts slowly ossify during the expansion process and therefore it was deemed an acceptable approximation to close them from the beginning.
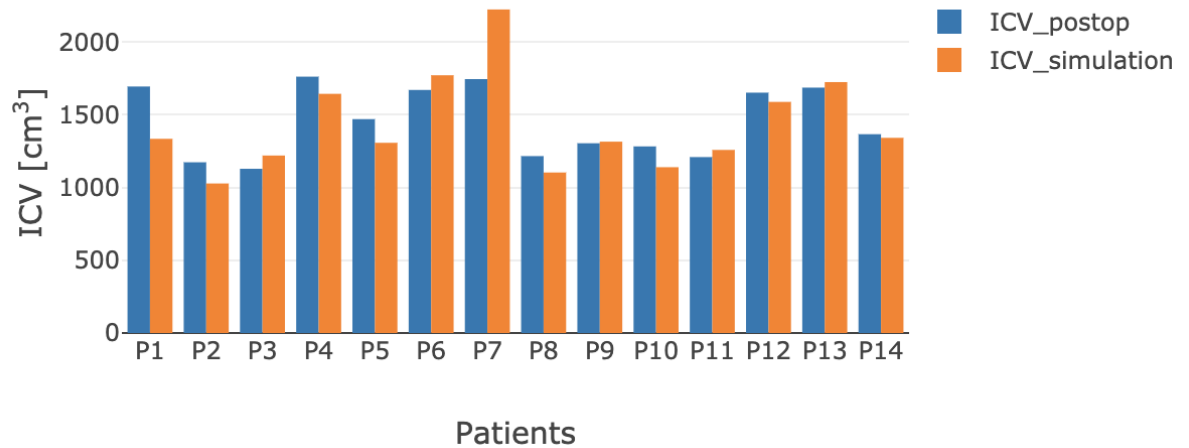

Figure 3.4: Comparison of the ICV calculated for the simulated model and post-operative CT for the 14 patients.

To analyse the agreement of our results, we carried out a Bland-Altman test. This is the most common method for comparing two measurements of the same variable, in our case, the postoperative ICV and the ICV predicted by the simulation. The resulting graph is a scatter plot XY, in which the X-axis shows the mean of the two measurements, and the Y-axis, the difference between those measurements [41].
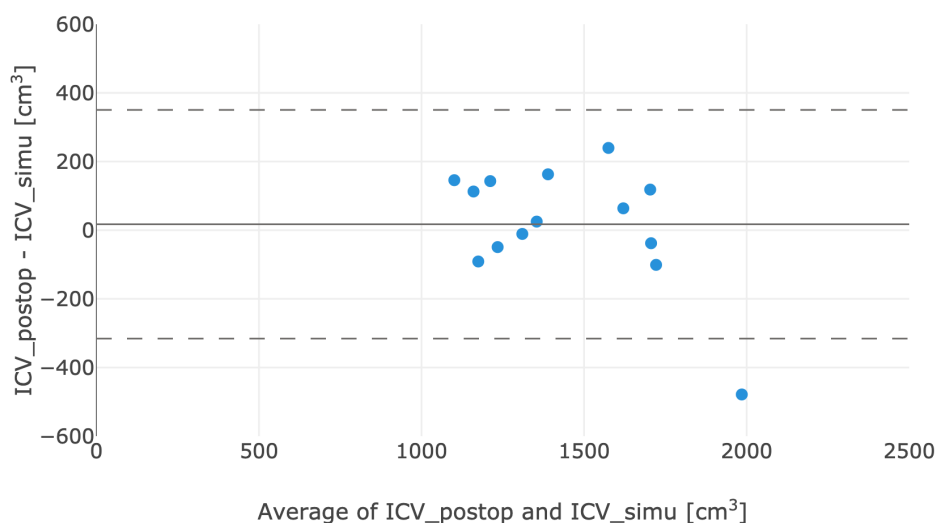

Figure 3.5: Bland-Altman plot of the whole population.

In Figure 3.5, three horizontal lines are represented. The bias (solid line) is computed as the mean of the values determined by one method minus the values determined by the other method and equals to 17.3 cm^3. Then the upper and lower limits of agreement (LOA) (dashed lines) are calculated by using that bias and the standard deviation (SD) of the differences between the two measurements such that 95% of the data should lie within ± 1.96 SD of the mean difference (bias). This corresponds to -315.8 and 350.4 cm^3 for the lower and upper limit respectively.

This type of graph can then highlight anomalies, for example, if one method always gives too high results, then all points are above or below the zero line. If the points on the Bland–Altman plot are scattered all over the graph, above and below zero, then it suggests that there is no consistent bias of one approach versus the other.

In our case, all data points are within the 95% confidence interval except one corresponding to Patient 7 as expected (below the lower LOA). If the differences within bias $\pm$ 1.96 SD are not clinically important, the two methods may be used interchangeably. We'll have to keep in mind that the simulated model ICVs were measured manually and therefore could contain small measurement errors.
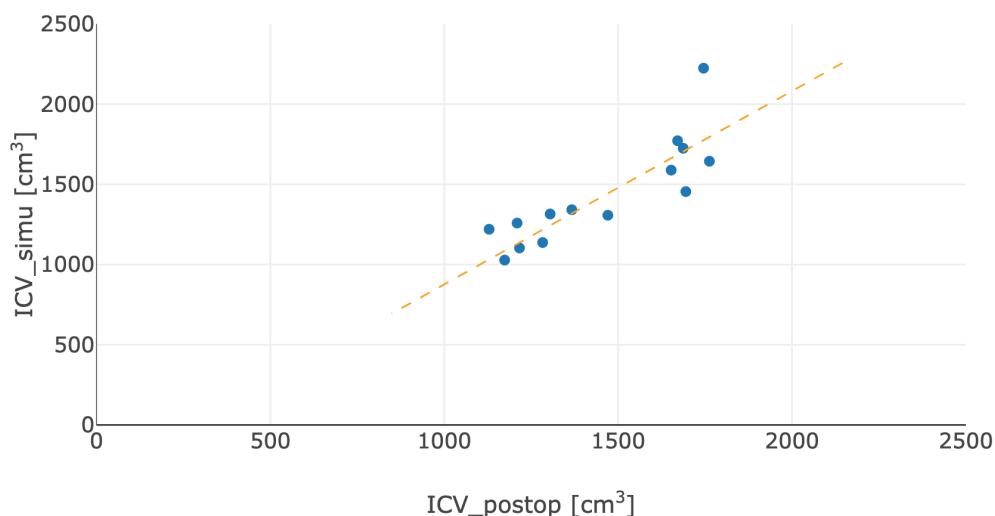

Figure 3.6: Correlation plot between the post-operative ICV and the simulated model ICV

Figure 3.6 shows, the correlation between measurements of the ICV from the postoperative CT and from the simulated model. The correlation coefficient, r, measures the strength and the direction of a linear relationship between two variables. Its value is always between -1 (no relationship) and +1 (perfect positive relationship). Here, r equals +0.85 meaning that the relationship is fairly strong and the positive sign indicates that when one variable increases, the other one tends to increase as well [42].

Correlation coefficients have a probability, p-value, which shows the chances that the relationship between the two variables is equal to zero (null hypotheses i.e no relationship). Strong correlations have low p-values because the chance that they have no relationship is very low. In this case, the p-value is equal to 0.0002 which confirms that the correlation is statistically significant [42].

3.3   Cranial Index

The cephalic index or cranial index is the ratio of the maximum width of the head multiplied by 100 and divided by its maximum length. This ratio is the criterion used to classify the patient's head shape.

The indices are categorized in 3 main groups [43]: dolichocephalic or 'long-headed' below 75%, mesocephalic or 'medium-headed' between 75 and 83% and brachycephalic or 'short-headed' above 83%. This index was calculated in `Meshmixer` using the *Units & Dimensions* tool in the *Analysis* tab. This tool provides the width, length and height of the skull. It must be noted that for a relevant comparison with the CI of the postoperative CT, the latter has to be previously aligned with the model predicted by the simulation.

Patient	Syndrome	Simulated model			Postoperative CT			|Diff CI|
		Width	Length	CI (%)	Width	Length	CI (%)	
1	Apert	140.4	159.1	88.2	153.6	158.5	96.9	8.6
2	Cranial Dys.	131.5	141.9	92.7	146.9	143.7	102.2	9.6
3	Apert	128.7	136.8	94.1	131.3	135.2	97.1	3.0
4	Multi-sutural	153.4	168.2	91.2	155.8	168.9	92.2	1.0
5	Crouzon	130.2	158.0	82.4	140.3	161.6	86.8	4.4
6	Apert	141.8	170.3	83.3	146.7	166.0	88.4	5.1
7	Pfeiffer	156.2	164.8	94.8	155.9	138.4	112.6	18.1
8	Multi-sutural	125.9	156.6	80.4	131.0	157.6	83.1	2.7
9	Crouzon	121.1	182.0	66.5	128.4	176.1	72.9	6.4
10	Crouzon	136.4	150.8	90.5	135.2	156.4	86.4	4.0
11	Crouzon	121.5	180.1	67.5	126.9	183.0	69.3	1.8
12	Multi-sutural	133.4	176.2	75.7	141.1	175.0	80.6	4.9
13	Multi-sutural	145.1	188.4	77.0	150.3	188.8	79.6	2.6
14	Multi-sutural	119.8	162.4	73.8	131.0	161.4	81.2	7.4

Table 3.1: Dimensions of the skull in millimeters and cranial index computed from these measurements for the simulated models and postoperative CTs.

Based on the postoperative CI and the indices recovered from literature [43], the population of the study can be classified as 2 dolichocephalics, 4 mesocephalics and 8 brachycephalics.

By looking at the last column of Table 3.1 containing the difference between the CI computed for the postoperative CTs and the simulated models, it is possible to observe that difference between computed and measured CI ranges up to 8-10 %. Through a closer inspection, it is noticeable how the predicted length is very close to the measured one while the predicted width is around 10mm lower than that measured on the post-op 3D models. This may due to the presence of cranioplasty springs, which add width and render such measurements less reliable (Figure 3.7). The most extreme value difference is 18% corresponding to Patient 7, who had the smallest time period before his follow-up CT. The next chapter will consist in trying to optimize the material properties to fix these differences.
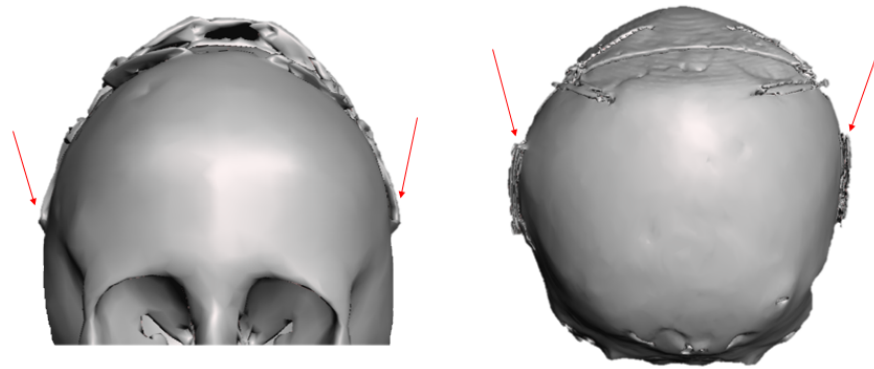
Figure 3.7: Cranioplasty springs viewed from the front and the back in the postoperative CTs of Patient 14 and 9 respectively.

Patient's information	Transverse plane cut	sagittal plane cut
Patient 1 Time surg. - CT: 162 days Crouzon		
Patient 2 Time surg. - CT: 67 days Crouzon		
Patient 3 Time surg. - CT: 29 days Crouzon		

Table 3.2: Illustrations of the comparison between the simulated models (dark grey) and the postoperative CT scan (light grey)
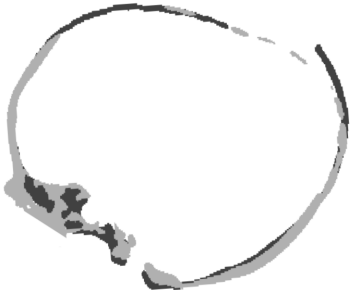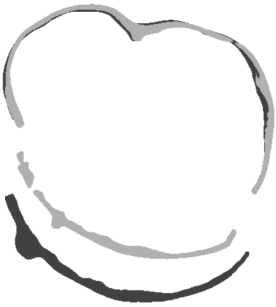
Patient's information	Transverse plane cut	sagittal plane cut
Patient 4 Time surg. - CT: 70 days Multi-sutural		
Patient 5 Time surg. - CT: 112 days Crouzon		
Patient 6 Time surg. - CT: 57 days Crouzon		
Patient 7 Time surg. - CT: 6 days Pfeiffer		

Table 3.3: Illustrations of the comparison between the simulated models (dark grey) and the postoperative CT scan (light grey) (continued)
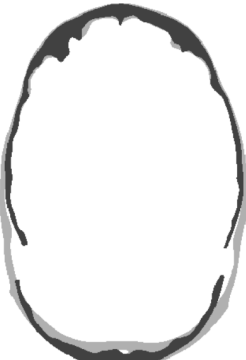
Patient's information	Transverse plane cut	sagittal plane cut
Patient 8 Time surg. - CT: 266 days Multi-sutural		
Patient 9 Time surg. - CT: 562 days Crouzon		
Patient 10 Time surg. - CT: 280 days Crouzon		
Patient 11 Time surg. - CT: 144 days Crouzon		

Table 3.4: Illustrations of the comparison between the simulated models (dark grey) and the postoperative CT scan (light grey) (continued)
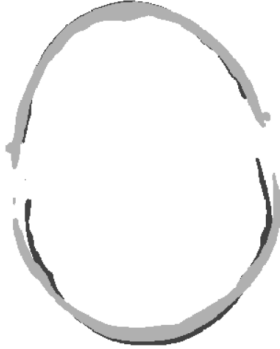
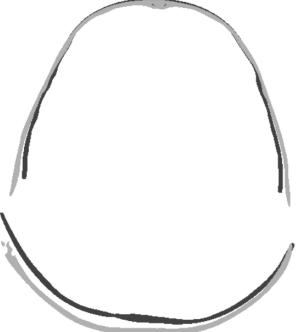| Patient's information	Transverse plane cut	sagittal plane cut
Patient 12 Time surg. - CT: 152 days Multi-sutural		
Patient 13 Time surg. - CT: 86 days Crouzon		
Patient 14 Time surg. - CT: 68 days Crouzon		

Table 3.5: Illustrations of the comparison between the simulated models (dark grey) and the postoperative CT scan (light grey) (continued)
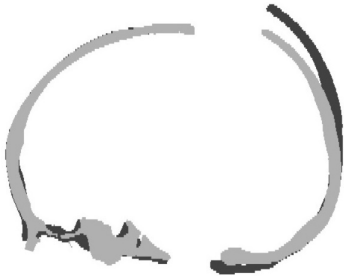
Chapter 4

Optimization : Spring Kinematics

4.1 Methods

4.1.1 Patient List

This part of the study includes 50 patients who had received a posterior vault expansion operation at Great Ormond Street Hospital between 2008 and 2016. The surgeries were performed by the craniofacial team under the lead clinicians Prof. David Dunaway and Mr. Owase Jeelani.
The list was limited to patients with 2 springs and an "hinged" PVE (in opposition to the "flap" PVE where a total craniectomy of the back of the skull is done).

4.1.2 Data collection for Patients

This part of the project required the use of a specific computer which can access the GOSH database containing every patient's available imaging and personal data.
For all 50 patients, the following information was collected:

- Patient number, depending on when they entered the study.

- Date of birth,

- Date of PVE procedure,

- Age at surgery was then calculated by subtracting the date of birth and the date of the operation,

- Number of postoperative follow-up images

4.1.3 Measurements

The spring opening measurements were taken manually for all patients at each postoperative follow-up to observe their extension over time. The amount of follow-ups and on-table measurements were unfortunately way smaller than for the previous studies on the sagittal craniosynostosis patients and a total of 80 X-ray images were collected. Patients who received a second PVE operation were excluded.
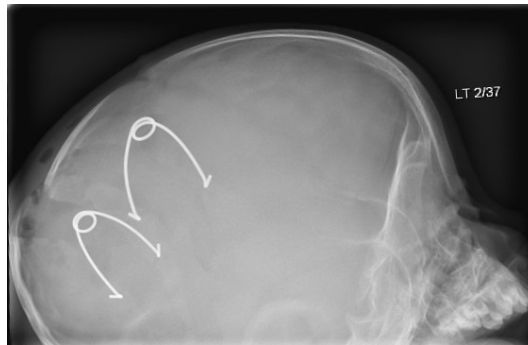
Figure 4.1: X-ray image of Patient 4 implanted with 2 lateral springs.

4.1.4 Measurement Methods

Since the measurements were taken from the database on two-dimensional images, we had to take into account the image projection and the curvature of the springs while measuring the distorted springs. The only way of being completely accurate is taking measurements in the operating room. Those data were not recorded for the PVE patients and therefore two approaches were considered to measure the springs opening (OP) from the available follow-up x-rays.

Method 1: Thales Theorem

Knowing that the real value of the ring diameter is 10 mm (Figure 4.2), the spring shape was approximated to a triangle and, by making sure to take measurements parallel to each other, we used the Thales theorem to retrieve an approximation of the real measurements of the distorted springs. From the theorem, we obtain the equation:

$$\frac{D_R}{D_F} = \frac{n_R}{n_F} \tag{4.1}$$

Where D_F is the real distance between the feet of the spring, D_R is the real diameter of the ring = 10 mm, n_F and n_R are the corresponding measurements on the distorted image (Figure 4.2). Therefore,

$$D_F = 10 \times \frac{n_F}{n_R} \tag{4.2}$$

Figure 4.2: Modelisation of a distorted spring (left) and a straight one (right).

Method 2: Phantom Measurements [44]

The second approach required a few more values and the mathematical models is presented below. First, the non-distorted angle α' value is computed,
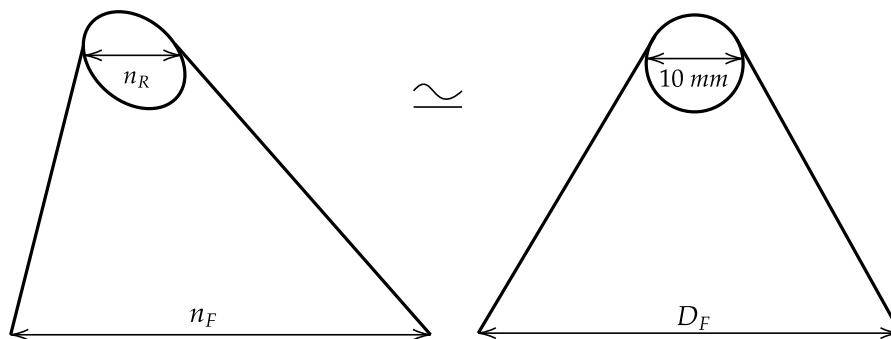
$$\alpha' = 2 \arctan \left(\frac{A_1}{B_1} \tan \frac{\alpha}{2} \right) \tag{4.3}$$

with α being the opening angle, A_1 is the vertical length of the ring and B_1, the horizontal length of the ring (Figure 4.3).

The second formula takes this α' and uses the length of the spring arms $L = 37$ mm (obtained through the Pythagorean theorem), to calculate the non-distorted spring opening OP:

$$OP = 2L \sin \left(\frac{\alpha'}{2} \right) \tag{4.4}$$
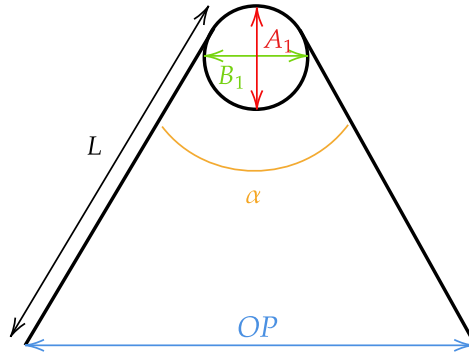
Figure 4.3: Schematic of the spring variables used in the Phantom measurements method.

Results of Both Methods

Both methods were applied to the 160 springs and all measurements were recorded in an `Excel` spread sheet.
Before looking at the results, it can be stated that the second method was very difficult to apply to each and every spring. Staying consistent in the measurement of the angle was especially challenging as some of the spring legs were bent on the image.

Now looking at Figures 4.4 and 4.5, the measurements obtained with the first method appear less dispersed and a larger portion of them belong to a realistic opening interval. Indeed, when the springs are placed during the procedure, their legs are crimped to an opening of about 20 mm and a fully opened spring reached an opening of 60 mm. In contrast, adjusted measurements obtained with the second method largely exceeded this interval as 11 points were above 60 mm and 22 points below 20 mm.
We can conclude that errors were introduced in the measurement adjustments with the second method and as a result, the first one was chosen to continue the kinematic analysis.
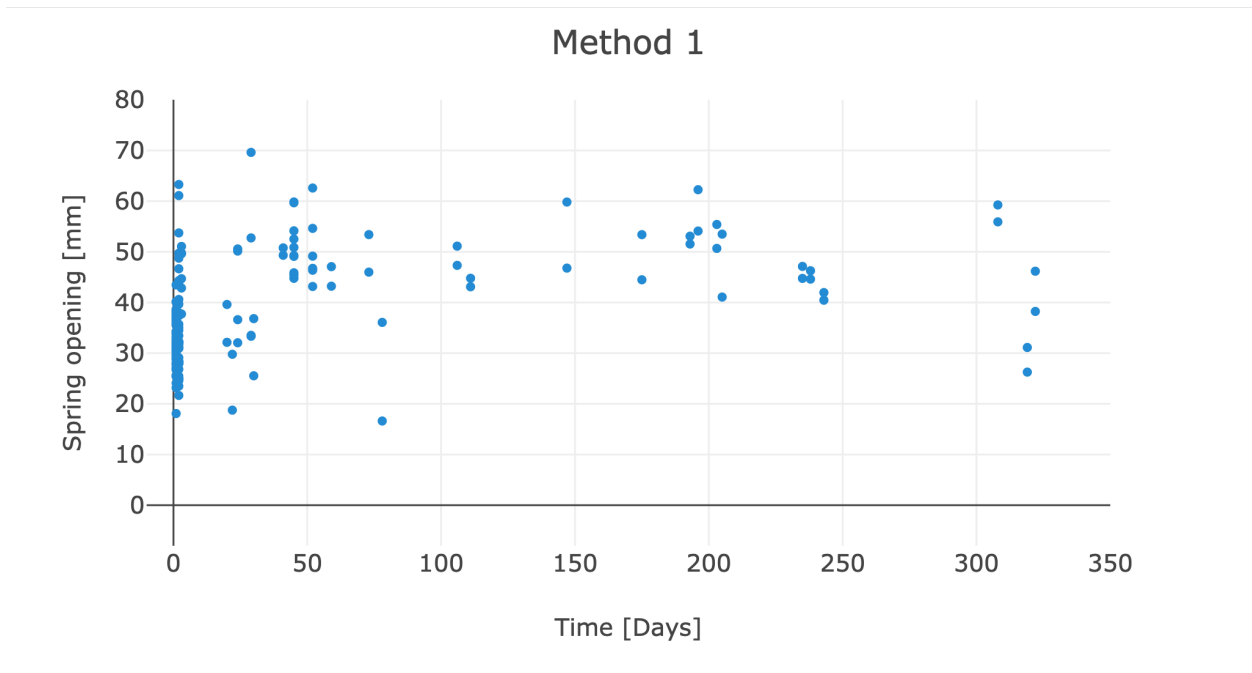
Figure 4.4: Adjusted measurements of both springs for the 80 images over time with the Thales theorem.
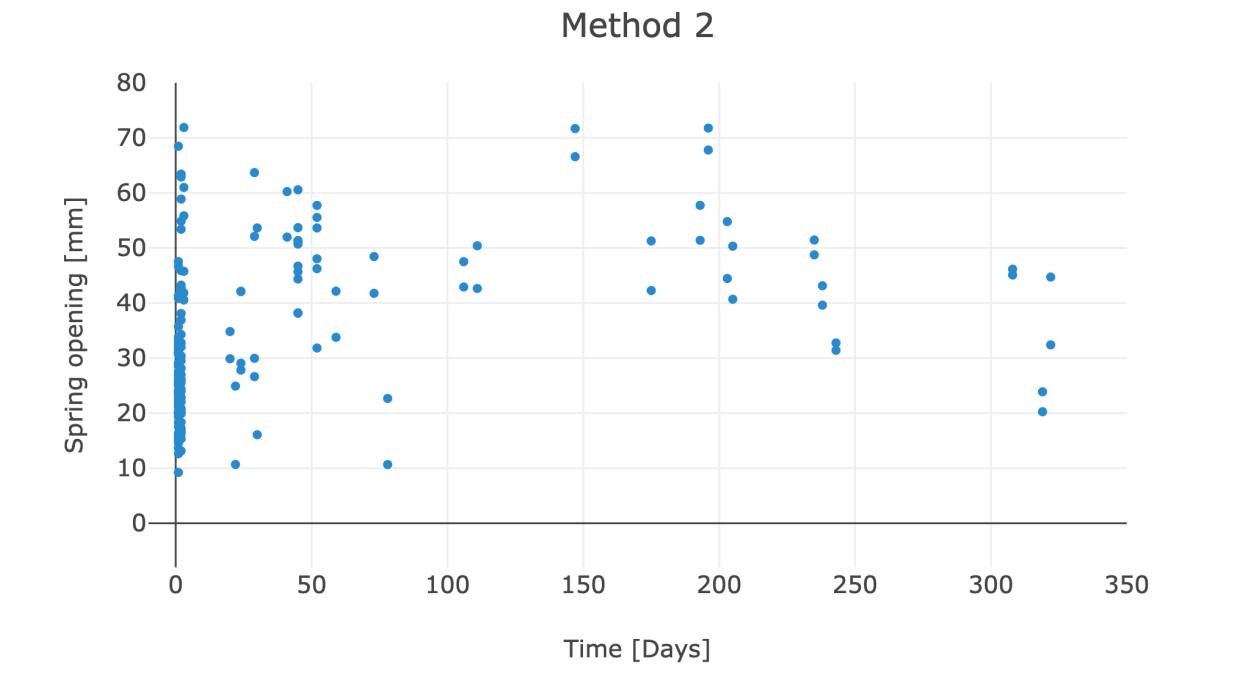
Figure 4.5: Adjusted measurements of both springs for the 80 images over time with the Phantom measurements.

4.2 Data Analysis

The aim of this section is to create the line of best fit of Figure 4.4 in order to assess and quantify the spring opening kinematics relative to PVE procedures.

4.2.1 Classification of the data

The spring opening data was simplified by taking into account only the average measurement of the two spring for each patient. The measurements were than divided in 4 groups representing the follow-up (FU) images at different points in time:

- FU1 = [1-2] days, mean = 1.5 ± 0.5

- FU2 = [3-30] days, mean = 20.4 ± 10.5

- FU3 = [41-73] days, mean = 52.7 ± 11.8

- FU4 = [106-308] days, mean = 206.3 ± 65.1

For each group, the average opening and standard deviation were calculated, see Table 4.1 and illustrated in Figure 4.6.

	FU1	FU2	FU3	FU4
Average OP [mm]	32.6	40.6	50.2	49.1
SD [mm]	4.4	9.9	4.8	5.5

Table 4.1: Average opening and standard deviation calculated over time.

Figure 4.6: Average opening and standard deviation represented by follow-up.

4.2.2 Outliers Determination

Some outliers were removed from the graph to try and reach the best and most realistic approximation.

Outliers are defined as date values that differ greatly from the majority of the data set. The approach used is the Interquartile Range. It is based on the first (Q1) and the third (Q3) quartile of the the measurement data. Those are ea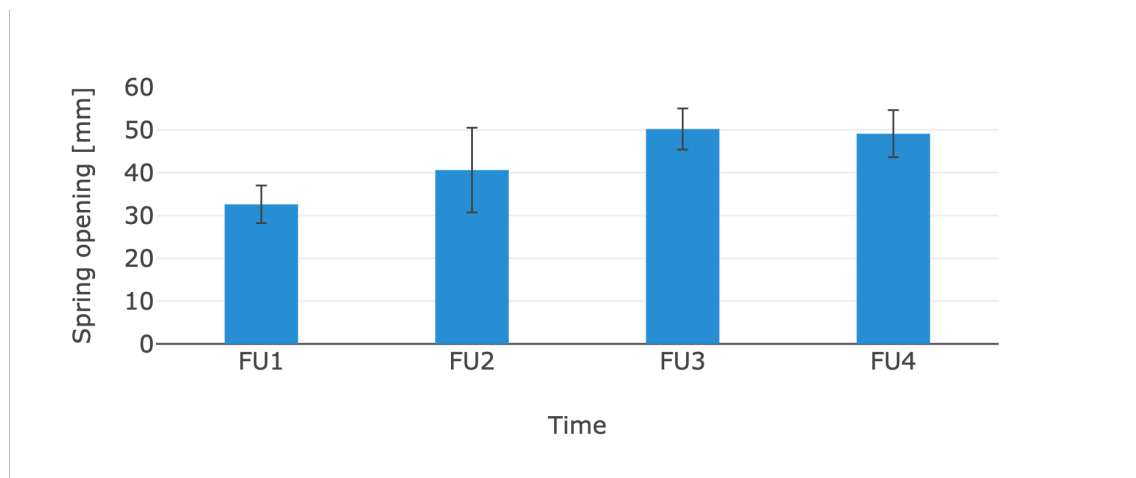sily computed with the *Quartile* operation in `Excel` and the Interquartile Range (IQR) is therefore the difference between these two calculations. The outliers were defined as those data points outside the range [Q1-1.5IQR, Q3+1.5IQR] [45].

In our case, the results obtained are listed in Table 4.2. In the end, two outliers were rejected from the group FU1 as their values were higher than 41.86 millimeters.

	FU1	FU2	FU3	FU4
Q1	29.9	34.1	46.3	45.4
Q3	34.7	45.6	53.1	53.1
IQR	4.8	11.5	6.8	7.6
Lower Limit	22.8	16.7	36.1	34.1
Upper Limit	41.9	62.9	63.3	64.4

Table 4.2: Computation data for outliers determination.

4.2.3 Mathematical Model

To create the line of best fit for our scatter plot, the *curve fitting tool* of `Matlab` was used.

This fitting was performed using the equation of an exponential rise (Eq. 4.5)[31] following a non-linear least squares method and the Trust-region algorithm. The robustness was chosen as Least Absolute Residuals (LAR); This method finds a curve that minimizes the absolute difference of the residuals, rather than the squared differences. Therefore, extreme values have less influence on the fit [46].

$$OP(t) = OP_0 + (OP_\infty - OP_0) \times (1 - e^{\frac{-t}{\tau}}) \tag{4.5}$$

Where,

- OP_0 is the initial spring opening,

- OP_∞ is the maximal opening which, in this case, is the opening at the last follow-up i.e. 49.1 mm (Table 4.1).

- τ is the time constant of the exponential (after a time equal to τ, the exponential rise has reached 67% of its maximum).

4.2.4 Curve Fitting Results

The result of curve fitting are presented with a 95% confidence interval in Table 4.3 and illustrated in Figure 4.7.

General model	OP_0 [mm]	τ [days]
	31.37 (30.84, 31.90)	21.21 (17.85, 24.58)

Table 4.3: Results for the general model.

Goodness of fit	R-squared	RMSE
	0.9749	1.574

Table 4.4: Goodness of fit.
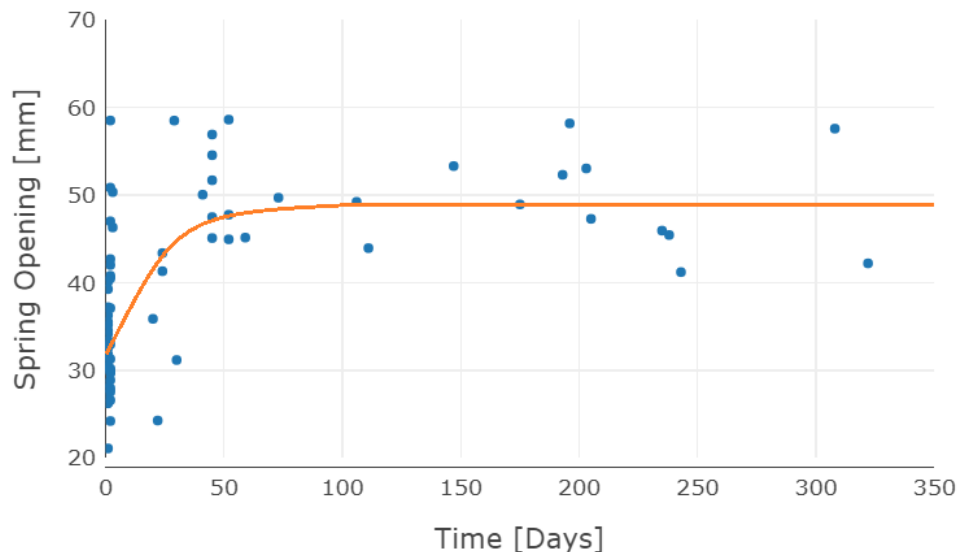
Figure 4.7: Fitting of the spring expansion scatter plot by the exponential model.

The values in Table 4.4 express that the fitting is actually of good quality as the R-squared value is very close to 1 and the Root Mean Squared Error (RMSE) is relatively small. An R-square value of 0.9749 means that the fit explains 97.49% of the total data variation about the average; it is the square of the correlation between the response values and the predicted response values [47].

Previously it was said that to assess the timing of the spring kinematics, two properties of exponential rise have been taken into account [31]:

1. The exponential function reaches its plateau after 5τ

2. In a normal distribution (mean, μ and standard deviation, σ), according the Chebychev's inequality, 97.8% of the population is found within the interval $[-\infty, \mu + 2\sigma]$.

Knowing that, it can be concluded that 97.8% of spring will reach the opening plateau after a time: $T = 5(\mu_\tau + 2\sigma_\tau)$.

However, contrary to the spring kinematics of sagittal craniosynostosis correction, this value of time relaxation τ was not computed for each patient individually because of the lack of follow-up information per patient. In our case, the value of τ was computed over the whole population to exploit at best the data available.

Therefore, with a time constant of 21.21 days, we can expect the springs to be fully extended after about 5τ, which represents 106 days.
By looking at the curve fitting results, one can deduce that over 60 days, the expansion has already reached over 98% of its final opening. We will thus be looking at the patients having a postoperative follow-up under 60 days to see if the optimization of our model can be validated.

Chapter 5

Effect of Kinematics Optimization

Three patients of the study had a time period between the procedure and the CT, lower than 60 days: Patients 3, 6 and 7 with 29, 57 and 6 days respectively.

For this new set of simulations, the constants relative to the bone, previously retrieved from literature [33] (see Section 2.2.8), were thus divided by 1.1 (corresponding to the time constant for the sagittal craniosynostosis case) and multiplied by 21.21 [days] (time constant arising from the kinematics optimization). The relative moduli remained unchanged. The viscoelastic properties of the skull therefore became:

Index i	Relative moduli (i)	Relaxation time (i) [s]
i=1	0.73213	1.296×10^5
i=2	0.25208	7.774×10^5

Table 5.1: Updated viscoelastic properties of the skull.

5.1 Simulations

From a visual inspection, it is visible from Table 5.2, that the use of the new material parameters allow for dramatic improvement in the simulation of spring expansion. The table presents a sagittal and a transverse plane cuts showing that the predictions match the postoperative CTs very closely. The mismatch observable on the top of the skull is due to surgical repositioning of the top part of the occipital bone, with the aim of further improving the overall appearance. Such manual repositioning wasn't taken into account in the numerical prediction.
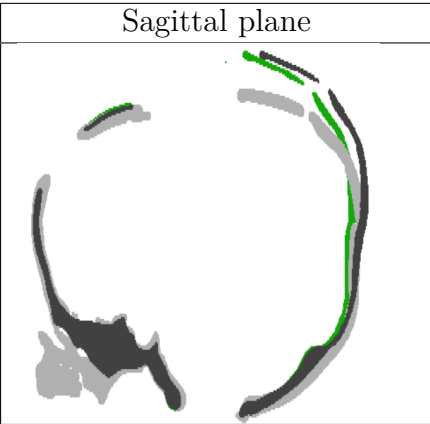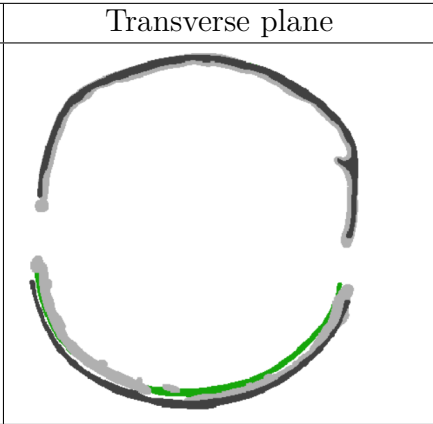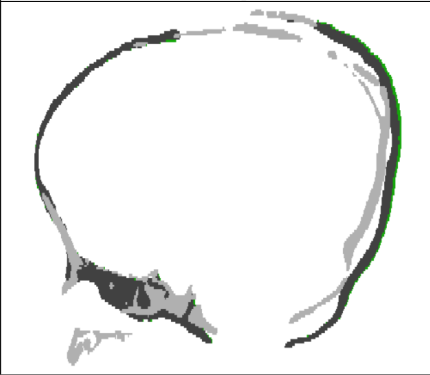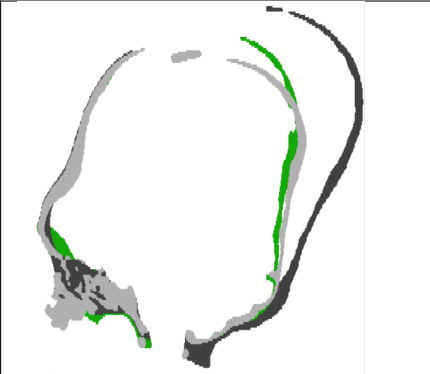
Patient's information	Sagittal plane	Transverse plane
Patient 3 Time surg. - CT: 29 days Crouzon		
Patient 6 Time surg. - CT: 57 days Crouzon		
Patient 7 Time surg. - CT: 6 days Pfeiffer		

Table 5.2: Illustration of the comparison between the simulated models (dark grey) and the post-operative CT scans (light grey) with the optimized kinematics (green).

5.2   Intracranial Volume

Figure 5.1 shows the variation of the intracranial volume before and after the optimization compared to the postoperative one. One can observed that the difference between the simulated and the postoperative model is decreased dramatically for Patient 7.

For the two other cases, a small but evident improvement is present. The error compared to the postoperative 3D image for each patient is very small and can be neglected. Indeed, Patient 3 had an error of about 2% of the postoperative ICV, Patient 6 had an error inferior to 5% and 2% as well for Patient 7.
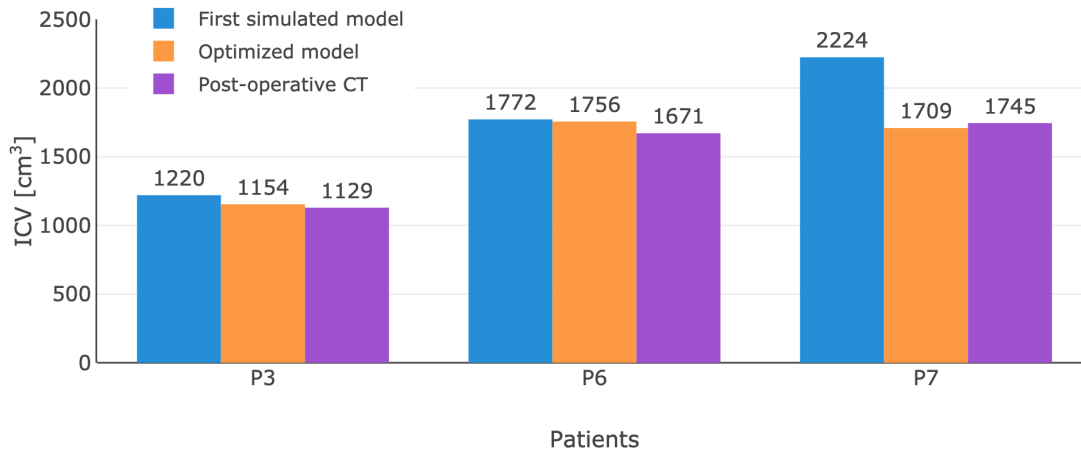
Figure 5.1: Bar graph illustrating the comparison between the ICV of the simulated models and postoperative CTs.

Once again, the results were analysed using a Bland-Altman plot (Figure 5.2) and a correlation plot (Figure 5.3). The first figure shows that the 95% confidence interval has been narrowed down and the majority of the data points are close to the average line meaning that the model predicts the volumes correctly.
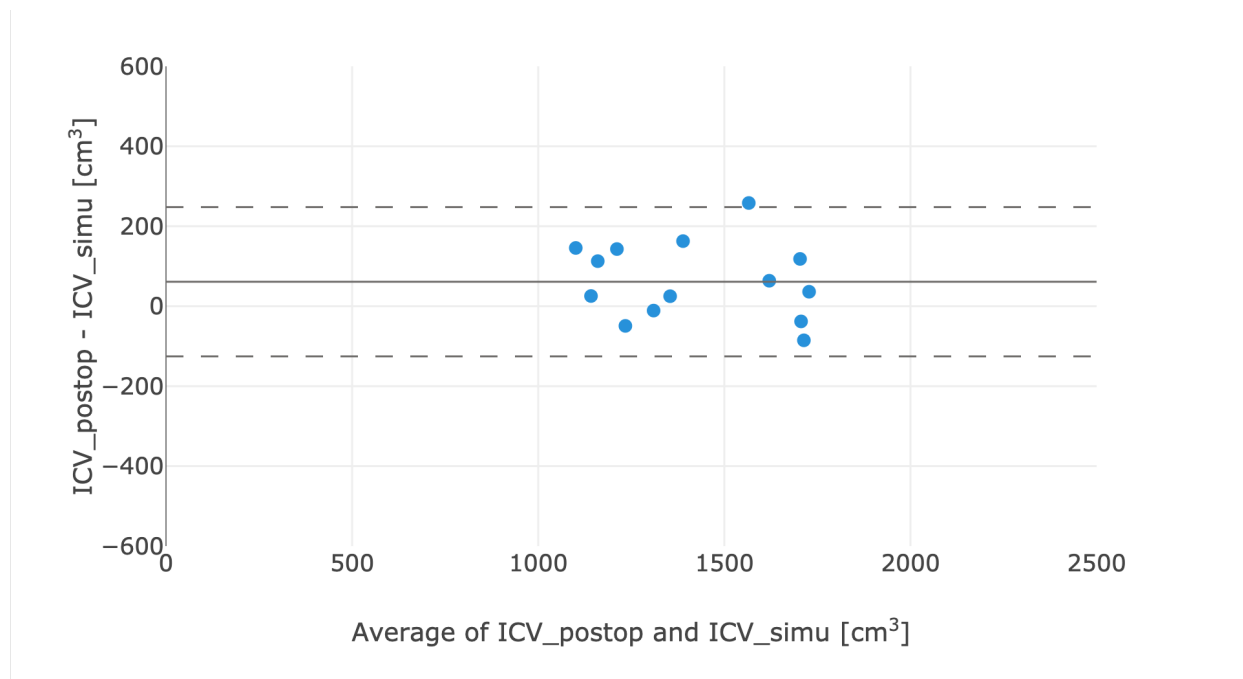
Figure 5.2: Bland-Altman plot including the optimized models

The correlation plot displays an even stronger correlation between the two measurements with a correlation coefficient r = +0.92 and a p-value of 2.3×10^{-6}.

These results allow us to validate the model as a good prediction tool in terms of intracranial volume.

Figure 5.3: Correlation plot between the post-operative ICVs and the simulated model ICVs optimized

5.3 Cranial Index

Finally, by looking at Table 5.3, one can see that this optimization also improves the estimation of the cranial index by reducing the value differences with the postoperative CTs. This means that the ratio between the width and the length of the patient's head is, in fact, closer to reality.

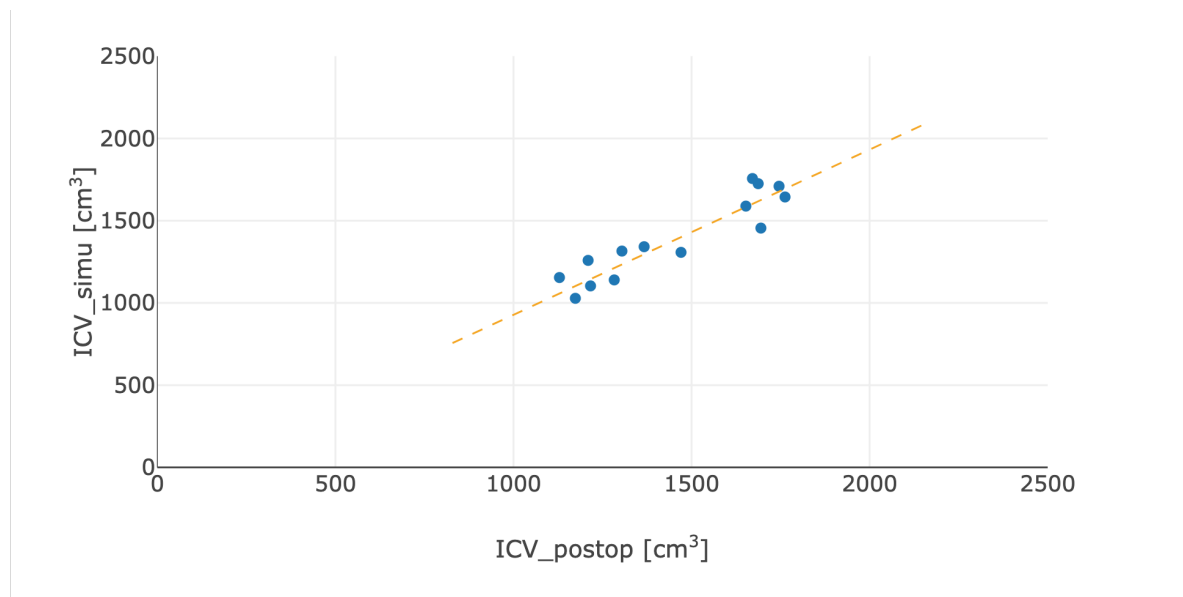| Patient	Syndrome	Simulated model			Postoperative CT			| Diff CI|
		Width	Length	CI [%]	Width	Length	CI [%]	
3	Apert	127.7	132.9	96.1	131.3	135.2	97.1	1.0
6	Apert	146.6	167.9	87.3	146.7	165.9	88.4	1.9
7	Pfeiffer	154.4	134.5	114.8	155.9	138.4	112.6	2.2

Table 5.3: Dimensions of the skull in millimeters and cranial index computed from these measurements for the simulated models and postoperative CTs after optimization.

5.4 Discussion

A major limitation of this work was the use of the same Young's modulus (1300 MPa) for the whole population, having an age range from 5 months to 5.5 years. Our choice was based on the average age of 2 years. It is well known that the skull stiffness varies when the baby grows up, going from soft in the early stages to stiff after a few years. It is well-known that the skull stiffness for our younger patients is likely to be less than the chosen value, however this would provide a marginal improvement to the model. Furthermore, literature data on calvarial stiffness is relative to normal subjects [48], therefore the mechanical properties of patients affected by syndromic craniosynostosis is - to date - unknown.

Chapter 6

Future Works: Analysis of Fracture due to Springs Insertion

It appeared that some patients' CTs scans (Figure 6.1) exhibited some cracking at the end of the osteotomy, where the forces were concentrated during the expansion process. Therefore, we wondered if those cracks would affect the final volume of the head and decided to add them in our models to see if they could be reproduced in simulations as this is something interesting to be able to control. Due to limited time and resources, the simulations were performed with unrealistic parameters but future developments will aim at ensuring simulation convergence in realistic conditions.
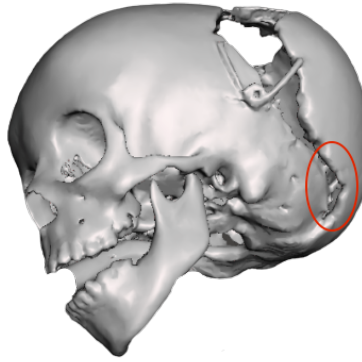
Figure 6.1: Parts of the cracking noticed in patients scans, hereby for Patient 13.

6.1   Basics of Fracture Mechanics

The fracture of a material involves a crack of a certain length which increases upon loading. The study of fracture mechanics is about understanding when a crack becomes critical i.e. when it reaches a sufficiently long length that the crack propagation goes from being stable to unstable. The latter will occur once the stress intensity factor (SIF) K exceeds the material's fracture toughness [49].
We can describe fracture mechanics using the equation below:

$$K = Y\sigma\sqrt{\pi a}$$

Where K is the Stress intensity factor [ksi$\sqrt{in}$] or [MPa$\sqrt{m}$], Y is a geometric factor being a function of the sample size and the size of the crack. σ is the stress applied and a, the crack length.

There are three ways of applying a force to enable a crack to propagate (Figure 6.2) [50]:

- Mode I is an opening mode where the force is perpendicular to the crack faces,

- Mode II is a sliding mode where crack faces slide on each other and the forces are parallel to the crack faces,

- Mode III is a shearing mode that involves a shear stress sliding the crack faces in the direction perpendicular to the primary crack direction.

A crack can be loaded in one mode exclusively, or it can be loaded in some combination of modes.
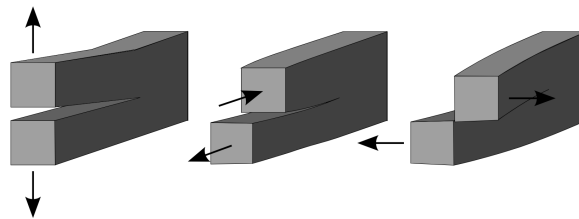
Figure 6.2: The three fracture modes [50].

6.2   Method

6.2.1   Crack Simulation Methods in `Ansys Workbench 19 R1`

For this part of the project, a recent `Ansys` feature was used: the Separating Morphing and Adaptative Remeshing Technology (SMART) crack growth, able to automatically remesh a 3D model during a simulation according to mesh propagation.
There are 2 fracture simulation methods available in the software and they rely on two different models [51] :

- The Cohesive Zone Modeling (CZM), used for simulating the debonding between two surfaces attached adhesively. The delamination occurs when a force is applied but cannot grow beyond the interface . This method will not be the first choice for simulating the crack growth in the bulk of a material [51].

- The eXtended Finite Element Method (XFEM), used for internal crack calculations. This method eliminates the need of remeshing the crack tip regions. Instead, it splits the elements in the zone to create a finer mesh without remeshing. However, this process is very computationally expensive and slow down the whole simulation [51].

In the case of SMART crack growth and unlike XFEM, the splitting area can be scaled up to larger projects because remeshing is limited to a small region around the crack tip at each iteration. [51]

6.2.2   Preparation in Simpleware: Creation of a Non-Uniform Rational Basis Spline (NURBS) Model

The model without osteotomy was prepared in `Simpleware`, every defect was smoothed and all the complex parts at the base of skull were be removed. Using the smoothing filters, the model was simplified as much as possible. The NURBS model was then created to later be imported in `Solidworks`. This technique was used to allow a very smooth surface and sharp cuts, which were not achievable with the usual method, in order to reduce the complexity and optimize the computation time in the simulation process. Once the full model generated, the geometry was divided in hopefully uniform patches. The process can be time consuming while trying to get a surface very smooth. The model was finally exported in a *.igs* files.

6.2.3   Replication of the Osteotomy in `Solidworks`

The file previously saved was imported in the software, it can then be modified by making cuts similar to the preoperative model used in previous simulations. For each part of the osteotomy, a new plane was defined in order to try and keep the cut as perpendicular to the surface as possible. This step is very important for the set-up of the crack in `Ansys`. Osteotomies were recreated from scratch and several iterations were used to ensure the bony cuts were as close to the original as possible. It was also necessary to create a sharp notch at the extremity of the osteotomy. The geometry was then saved as a *.SLPRDT* file.

Figure 6.3: Model with osteotomy before simulation (left) and model recreated in Solidworks (right).

6.2.4   Set-up in `Ansys Mechanical`

A static structural system was created with the imported geometry. For these simulations, it was deemed appropriate to use the sagittal plane of symmetry of the skull to considerably reduce the computation time. To achieve this, the geometry was opened in `Ansys Design Modeler`; up in the *Tool* tab, the *symmetry* tool was selected and the plane YZ was defined as the symmetry plane.

In `Ansys Mechanical`, the notch position had to be defined and the crack direction set up. For that, a new coordinate system was created and placed on the front edge of the notch. One axis had to be pointing forward to indicate the crack propagation direction (x), another axis normal to the notch's edge i.e. the crack opening direction (y) and the last one, aligned with the edge (Figure 6.4 left).

Figure 6.4: Set-up of the crack with the position of the coordinate system and the regions selected.

For the mesh, the method selected was the *Patch conforming method* using tetrahedrons elements of size 2 mm. Then using the *Sizing* tool, a sphere of influence of 6 mm of radius around the notch edge was created and centered on the coordinate system previously defined. The elements inside this sphere had a size of 0.08 mm (Figure 6.5).

Then, from the Command ribbon, the option for *Fracture* was chosen. Further options for introducing a crack were: Arbitrary Crack; Semi-Elliptical Crack and Pre-Meshed Crack. Here a *Pre-meshed Crack* had to be defined. To do that, three new named selections were created: *crack* on the edge of the notch, *top* on the superior face of the notch and *bottom* on the inferior face (Figure 6.4 right). This time the worksheet method was selected as each of these regions had to be associated to a node set for use in the analysis. The table was filled similarly to Figure 6.6 depending on the selection type.
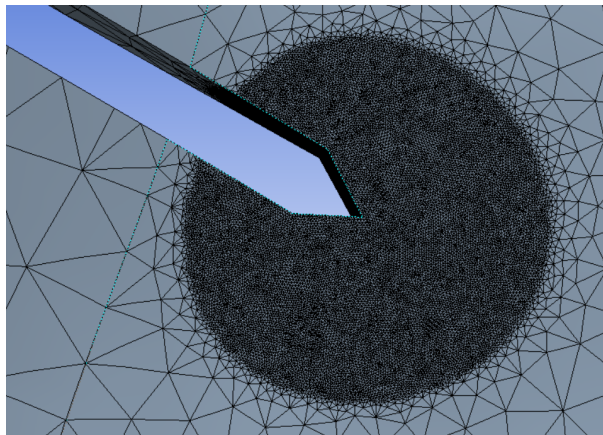

Figure 6.5: Premeshed crack with a finer mesh delimited by the sphere of influence

Within the Pre-Meshed Crack object, the Node sets created previously were allocated to the crack front, and the top and bottom faces. The crack coordinate system was referenced and the number of solution contours was then set to 4. These contours are the "loops" through the mesh around the crack tip used to evaluate the Stress Intensity Factor by integrating the crack tip region strain energy.

	Action	Entity Type	Criterion	Operator	Units	Value	Lower Bound	Upper Bound	Coordinate System
☑	Add	edge or crack	Named Selection	Equal	N/A	crack, top or bottom	N/A	N/A	N/A
☑	Convert To	Mesh Node	N/A	N/A	N/A	N/A	N/A	N/A	N/A

Figure 6.6: Worksheet used to convert the named selections into mesh nodes.

Again in the *Fracture* menu ribbon, three methods were available to model the crack front and its growth: Interface Delamination, Contact Debonding and SMART Crack Growth that was chosen for the rest of the simulation. The Pre-Meshed crack object was selected, the option to carry out a *Static* analysis was chosen and the *Critical Fracture Toughness* was defined. The Stress Intensity Factor method was selected in this case meaning that the crack would propagate when the calculated SIF, K, exceeded the fracture toughness K_c. This calculation was done along the distributed crack front, and the distribution of the SIF would control the adapting crack front shape.

The base of the skull and the anterior symmetry plane were defined as *fixed supports* and one spring is inserted in the notch provided for this purpose. The spring was defined in the same way as in the previous simulations with a stiffness of 1N/mm.
The main fracture mechanism in this model was the crack tensile opening Mode 1, which calculates K_1. Finally, a crack extension probe was added to the solution to monitor the crack growth and produced an XY plot.

6.3   Results

Springs were placed one by one and then both at the same time to observe the differences in crack extension. Their individual stiffness was fixed to 1N/mm and their relaxation constants were arbitrarily chosen after trying, to no avail, the ones used in previous chapters. This failure was suspected to be due to a lack of computing power and/or resources in `Ansys`.

The results obtained still provide an interesting comparison in total deformation and crack extension for each spring placement.

Figure 6.7: Total deformation of the 3 different configurations: spring on the side (left), spring on the top (middle), both springs (right)

The maximal deformations are depicted in Figure 6.7: 11.4 mm (left), 15.3 mm (middle) and
23.6 mm (right). It appeared indeed that larger deformations happened when the force was applied
on the superior part of the skull.

These numbers were obtained after 1 day and a time step of 3600 seconds as this was the maximal
simulation time that could be reached with our resources. Ideally, the simulation should have been
run over 10 days to observe if the crack allowed a closer approach to the actual deformation of the
postoperative images.

Figure 6.8 shows the propagation of the cracks in each configuration from the inside and the
outside; the top spring gave a slightly straighter crack compared to the side spring crack which
was more curved. It could also be noticed that the crack propagated with an angle as it followed
a downward path viewed from inside and an upward path viewed from outside.

It was still early in the propagation process to state confidently that the behavior was the same
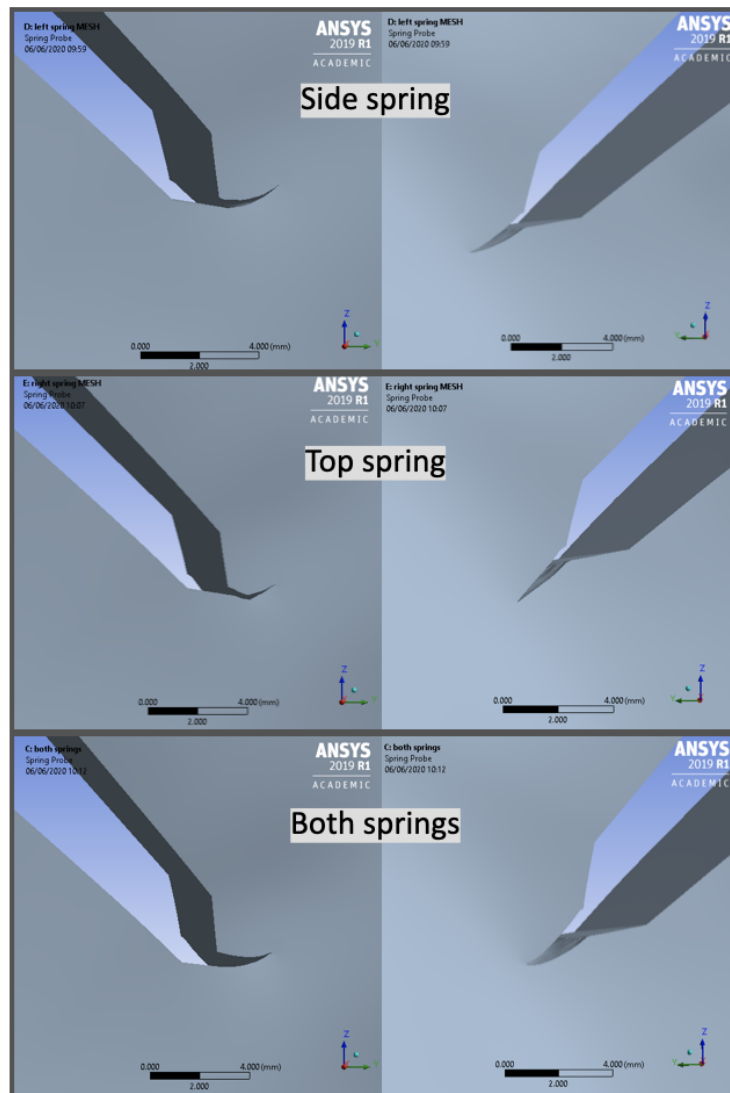than in the postoperative scan but the downward path in the inside is promising.

Figure 6.8: Inner (right) and outer (left) views for each configuration.

Finally, the extension lines were not strongly impacted by the placement of the springs. For all configurations, the fracture occurred at the same time and followed a similar course. It could be observed that when the two springs were involved, the fracture propagated quicker and further during the whole simulation time. This was however not a significant difference at this early stage since the scale was really small but it could show greater distinction after several days. Next to that, the extensions of the simulation for the top and side spring separately are almost completely overlapping.
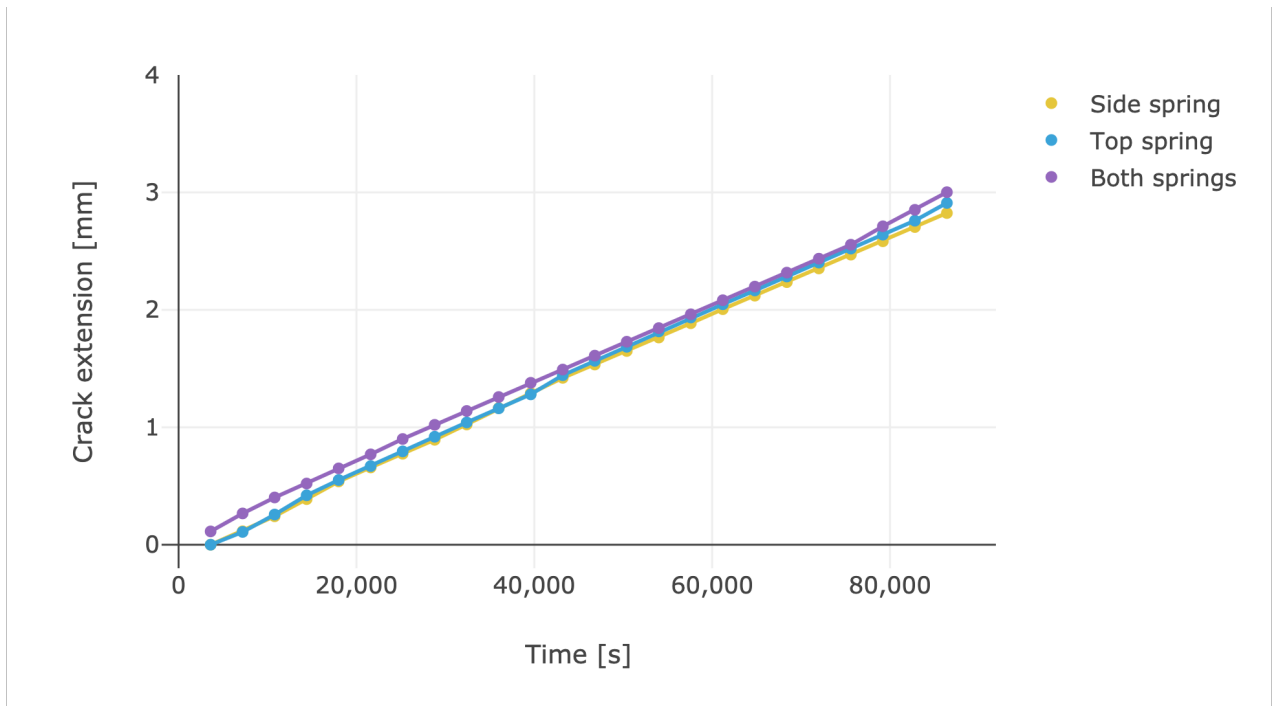

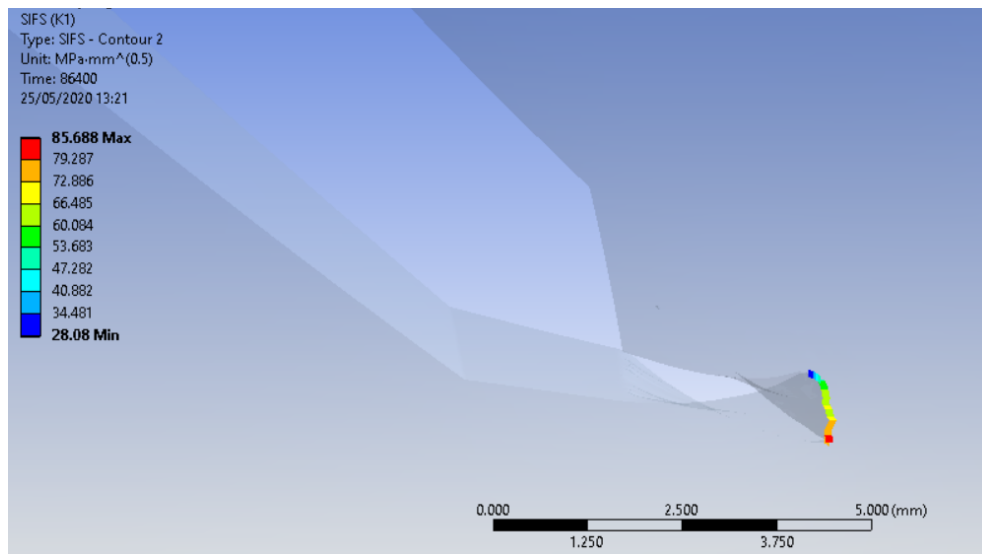Figure 6.9: Crack propagation for each configuration

Figure 6.10: Variation of the stress intensity factor across the crack edge

6.4   Limitations

The longest simulation which was finalised was over a day (86400 s, CPU time = 7 hours).
It was noticed that, although the software computed the first apparition of the crack in a consistent
way, the rest of the crack extension is strongly affected by the time-step adopted.
Furthermore, it appeared that fracture simulations in bent surfaces proved more difficult to con-
verge. This is one of the reasons the fracture was only simulated over a day. In future, extra
computational power will be needed to extend the simulation and allow for validation of the re-
sults. Our current achievements look - however - very promising.

Conclusion

The aim of this master thesis was to create a numerical model of spring assisted posterior vault expansion using finite element method based on pre- and postoperative images. Such models had already been created for sagittal craniosynostosis, therefore a starting point on spring kinematics was available. The ultimate goal was to be able to predict the post-operative shape of the skull based on surgical parameters (osteotomy location, choice of distractors) and time frame of postoperative assessment. Such model would constitute an invaluable surgical planning tool for clinicians but also a learning and training aid to teach new surgeons who approach craniofacial surgery.

First, the correlation between our model and the actual postoperative CT scans was highlighted, and comparison was drawn using intracranial volume and cranial index.
This first set of simulations was performed using a set of parameters retrieved from the literature, which were relative to numerical models of sagittal craniosynostosis correction in babies aged 3-8 months old. Such parameter set proved suitable to predict long term outcomes in the cohort analysed, but it failed to predict short term reshaping for patients who had postoperative follow-up before 60 days from the operation.
The next step was therefore to modify and adjust the kinematics to the specific case of PVE procedures. In order to do that, two measurement methods were explored to take the image distortion into account. Once a specific method was adopted, the spring openings were recorded over time for a total of 50 patients. This data collection resulted in a population based spring expansion curve showing that 67% of the maximal opening was reached after 21 days for the PVE, opposed to 1 day for the sagittal, confirming our previous assumption.

In the next section, this new parameter set was tested on a subset of patients (three) who received early post-op CT (under 60 days): This final set of simulations proved the validation of the model, displaying a far better match over time, especially in the beginning of the expansion. Correlation between the postoperative measured and simulated ICV was further improved.
Finally, the first steps of crack propagation on a skull model were laid down and assessed. This mode of analysis proved to be promising in order to improve estimation of the skull under the effect of cranioplasty springs. Although full validation wasn't achieved, these results trigger new research questions and perspectives for future works in order to fully predict the behavior of the posterior vault expansion.

Appendices

The Figures 6.11 to 6.24 shows the preoperative CT (top left), the model with osteotomy before simulation (top right) and the combination of the post-operative CT with the simulated model (bottom left) for all patients. The sagittal and transverse plane cuts are composed of the post-operative CT (light grey), the simulated model (dark grey) and the pre-operative CT (yellow).
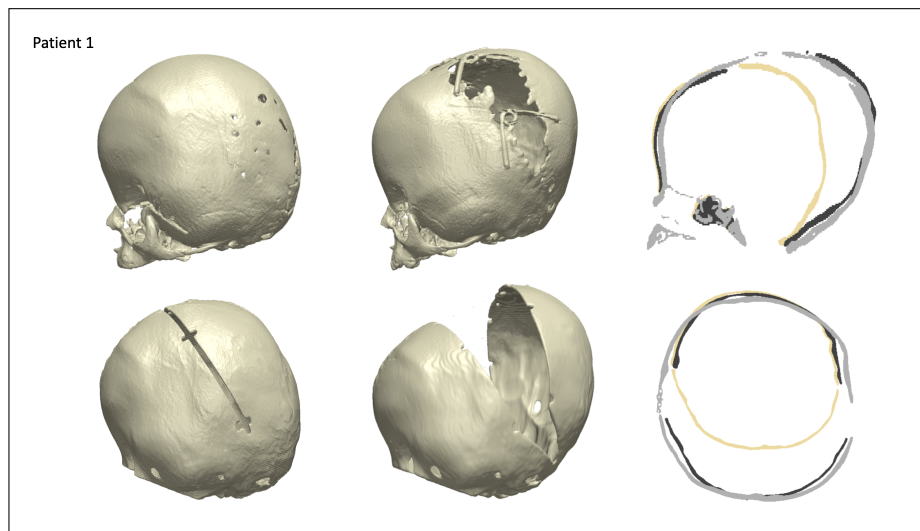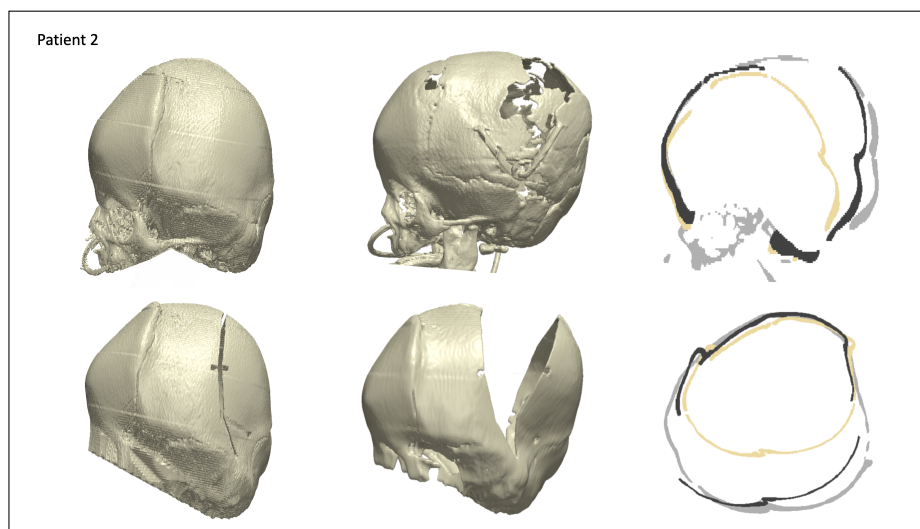

Figure 6.11: Patient 1
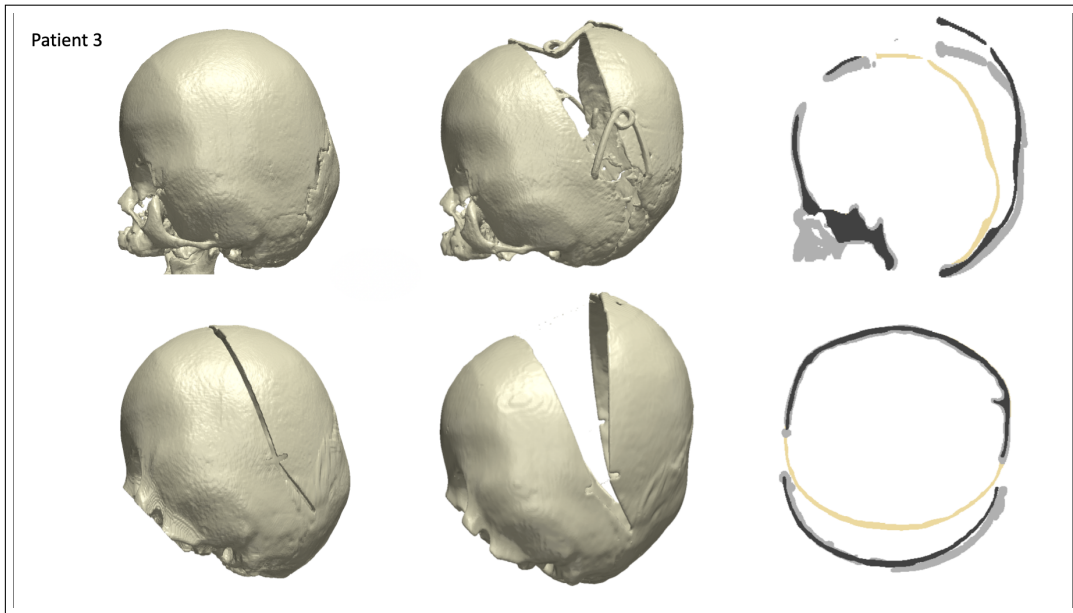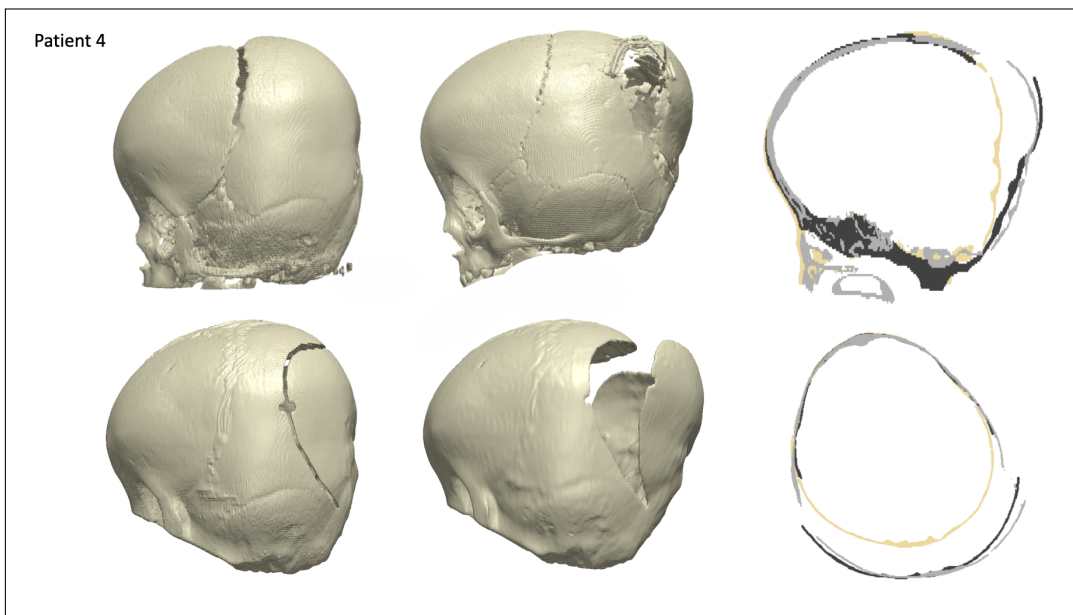

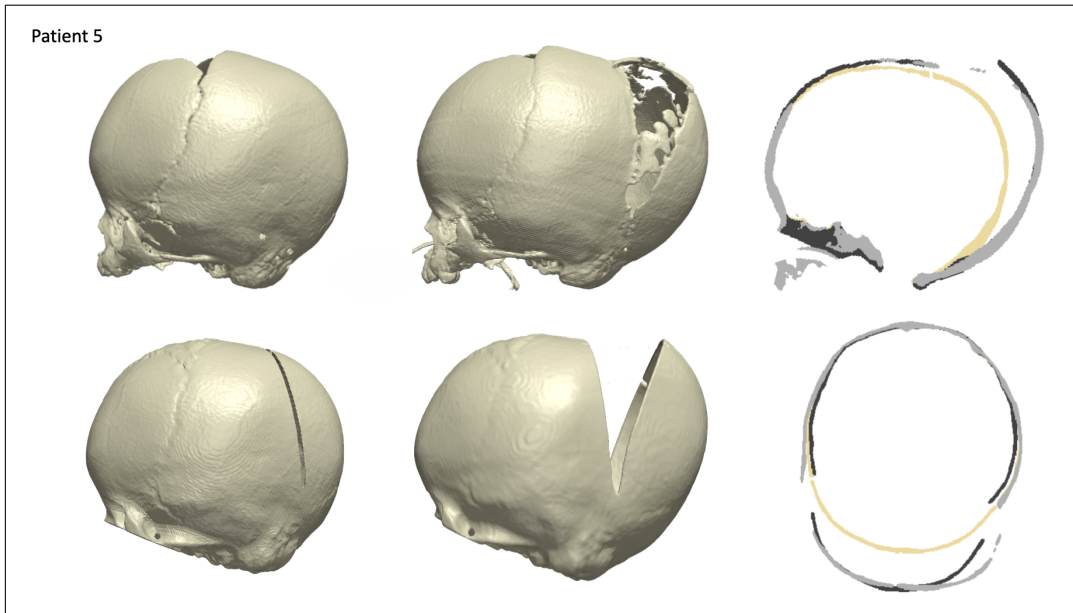Figure 6.12: Patient 2

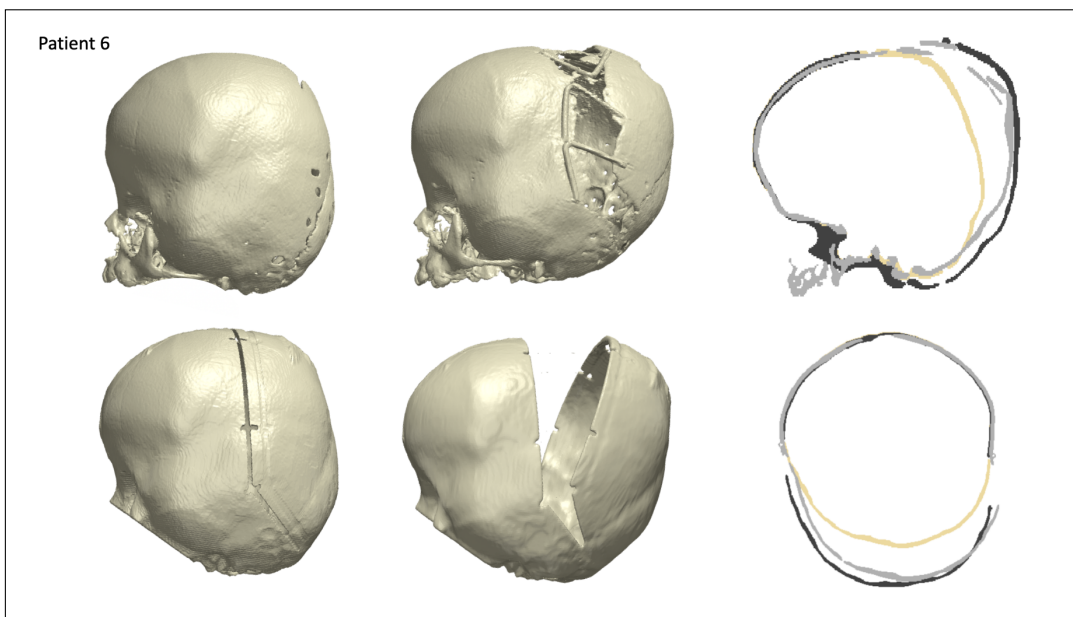Figure 6.13: Patient 3

Figure 6.14: Patient 4

Figure 6.15: Patient 5

Figure 6.16: Patient 6
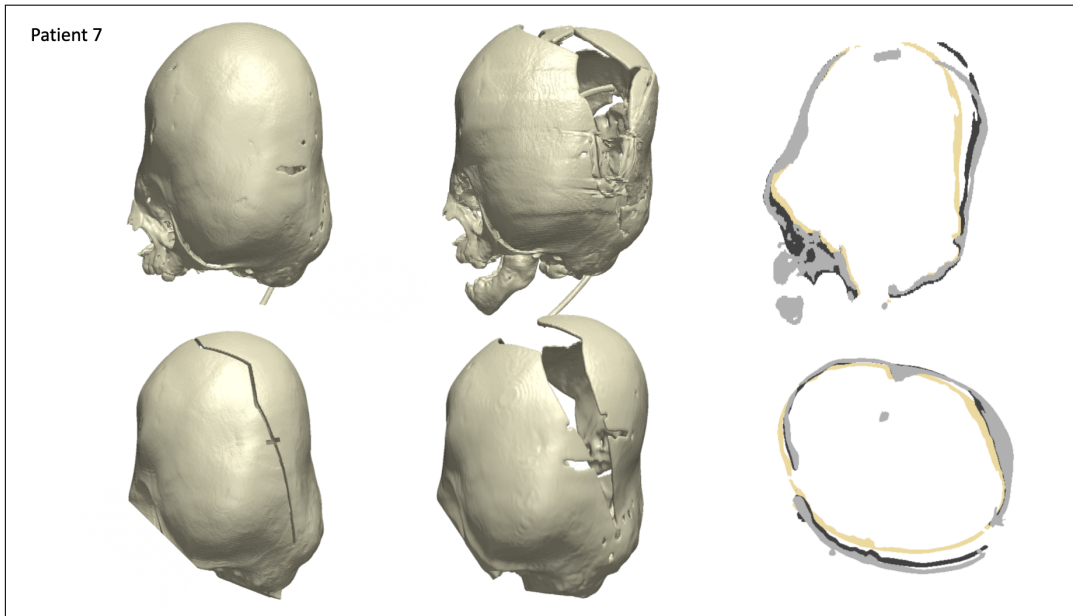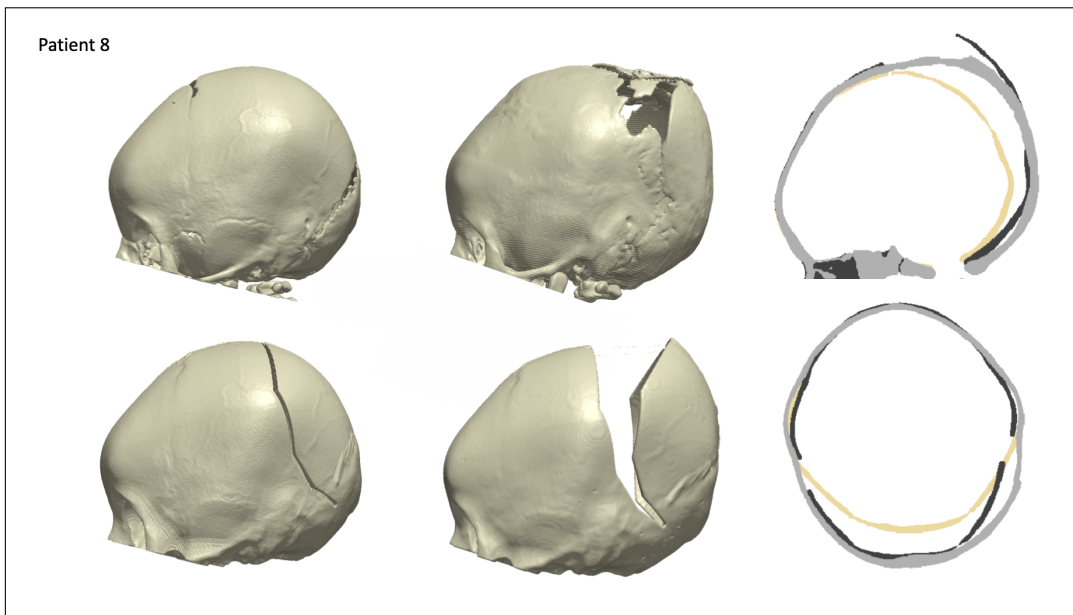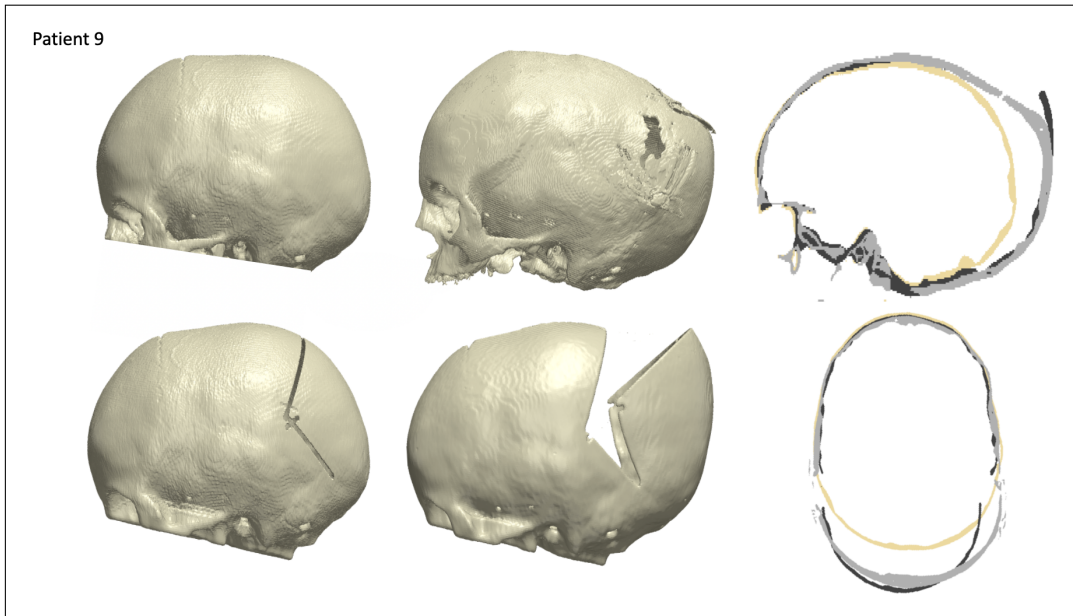
Figure 6.17: Patient 7

Figure 6.18: Patient 8

Figure 6.19: Patient 9

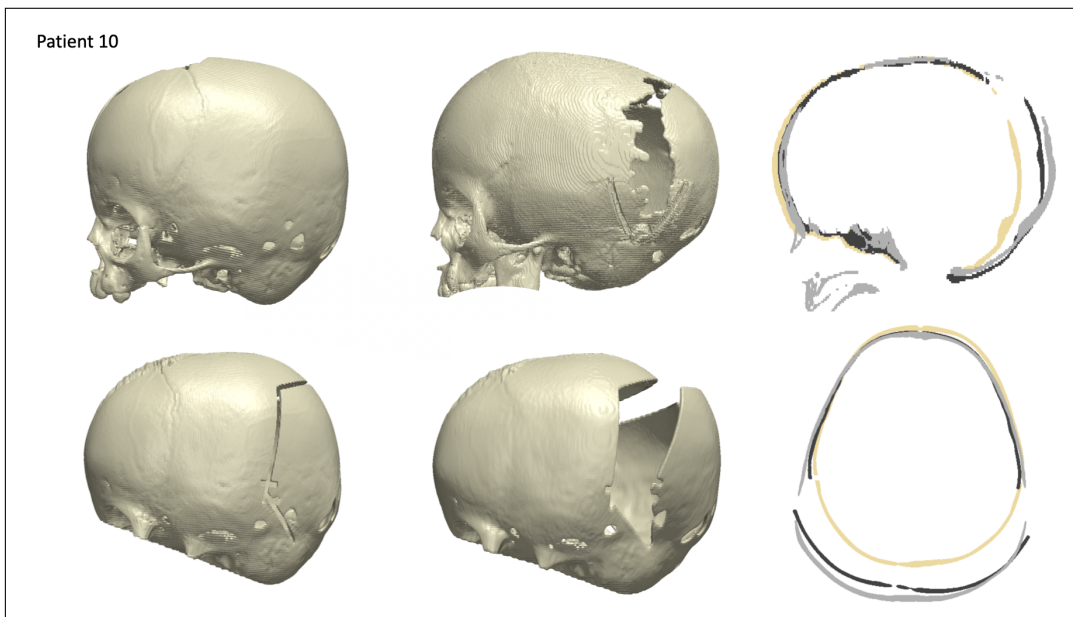Figure 6.20: Patient 10
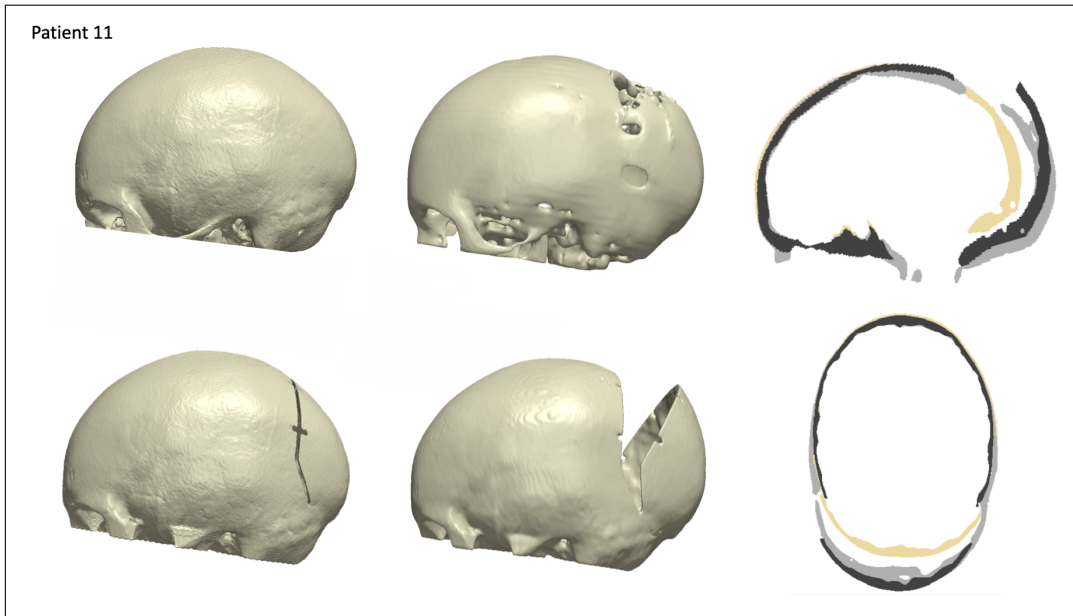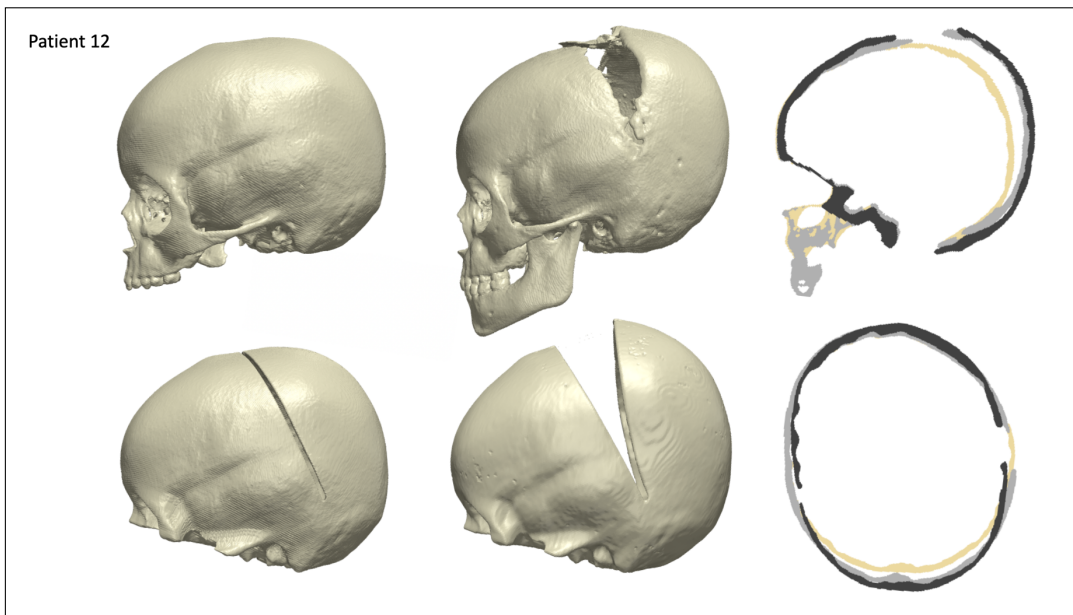
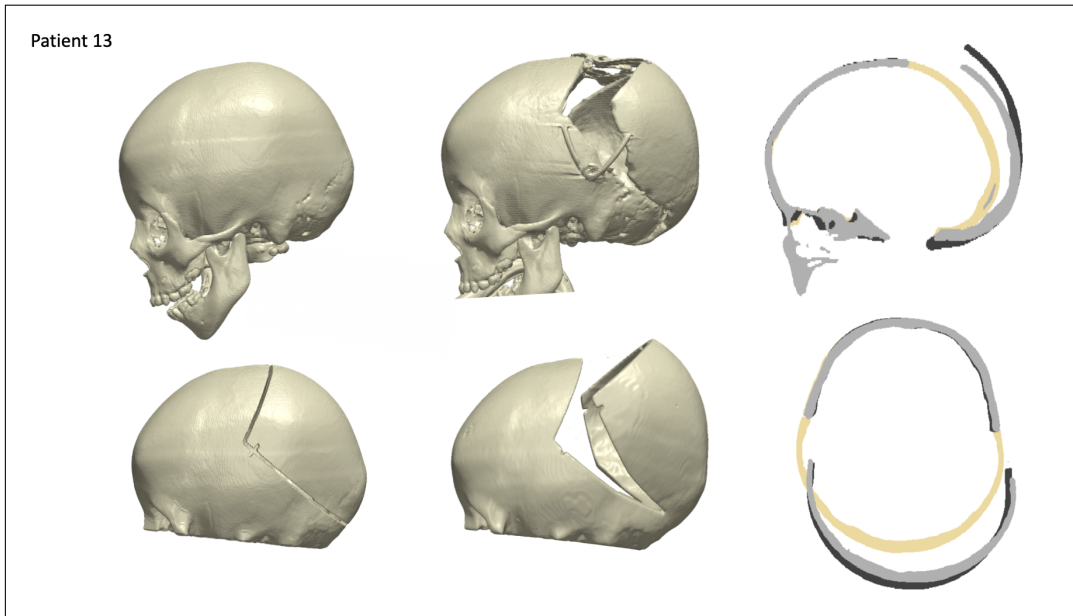Figure 6.21: Patient 11
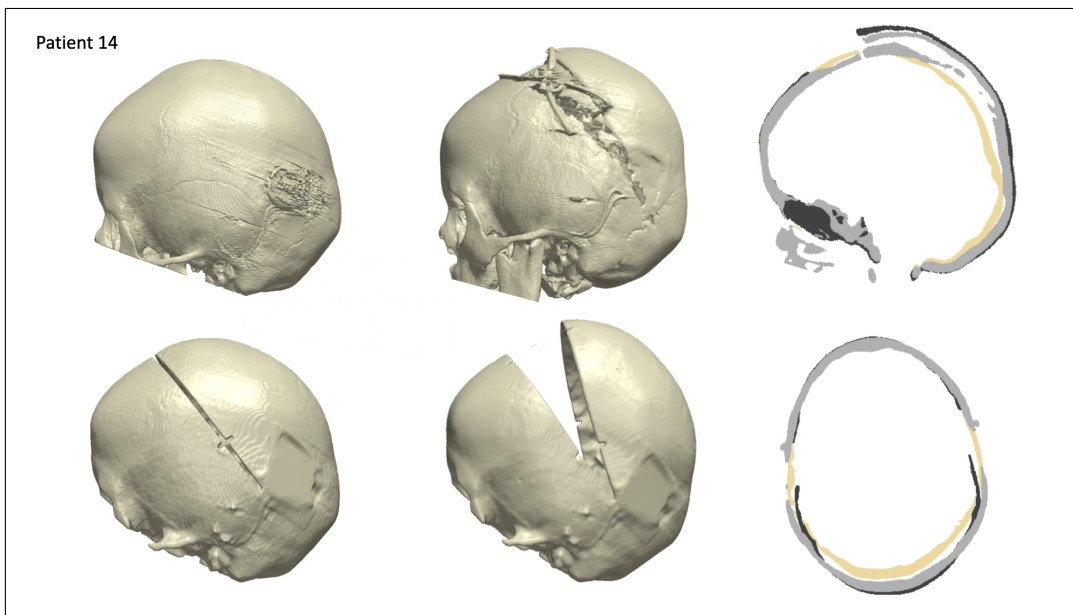

Figure 6.22: Patient 12

Figure 6.23: Patient 13

Figure 6.24: Patient 14

Bibliography

[1] Andrew W Hoey, Benjamin S Carson Sr, and Amir H Dorafshar. Craniosynostosis. *Eplasty*, 12, 2012.

[2] Kshemendra Senarath-Yapa, Michael T Chung, Adrian McArdle, Victor W Wong, Natalina Quarto, Michael T Longaker, and Derrick C Wan. Craniosynostosis: molecular pathways and future pharmacologic therapy. *Organogenesis*, 8(4):103–113, 2012.

[3] Skull. `https://en.wikipedia.org/wiki/Skull`. (Last accessed Feb 18 2020).

[4] The skull. `https://open.oregonstate.education/aandp/chapter/7-3-the-skull/`. Oregon State University, (Last accessed on Feb 18, 2020).

[5] Flat bone. `https://en.wikipedia.org/wiki/Flat_bone`. (Last accessed on May 31, 2020).

[6] Graham Lloyd-Jones. Ct brain anatomy: Skull bones and sutures. `https://www.radiologymasterclass.co.uk/tutorials/ct/ct_brain_anatomy/ct_brain_anatomy_skull`, 2019. (Last accessed on May 31, 2020).

[7] Basics of cranial anatomy and the nervous system. `https://www.goodmancampbell.com/brain-anatomy`, 2008. (Last accessed Feb 18, 2020).

[8] About the fontanelle. `https://www.pregnancybirthbaby.org.au/about-the-fontanelle`, 2018. (Last accessed on Feb 19, 2020).

[9] Anterior fontanelle. `https://www.earthslab.com/anatomy/anterior-fontanelle/`. (Last accessed on Feb 18, 2020).

[10] Tracy Jones. Bone matrix. `https://www.orthobullets.com/basic-science/9003/bone-matrix`, 2016. (Last accessed on April 15, 2020).

[11] Bone development & growth. `https://training.seer.cancer.gov/anatomy/skeletal/growth.html`. (Last accessed on Feb 19, 2020).

[12] Growth & formation of bone. `http://msgallagherlhs.weebly.com/formation--growth-of-bones.html`. (Last accessed on Feb 18, 2020).

[13] John C Kolar. An epidemiological study of nonsyndromal craniosynostoses. *Journal of Craniofacial Surgery*, 22(1):47–49, 2011.

[14] Rohit K. Khosla Rebecca M. Garza. Nonsyndromic craniosynostosis. *Semin Plast Surg*, 26:53–63, 2012.

[15] Kevin Flaherty, Nandini Singh, and Joan T Richtsmeier. Understanding craniosynostosis as a growth disorder. *Wiley Interdisciplinary Reviews: Developmental Biology*, 5(4):429–459, 2016.

[16] Jung Min Ko. Genetic syndromes associated with craniosynostosis. *J Korean Neurosurg Soc*, 59(3):187–191, 2016.

[17] James Seaward Christopher Derderian. Syndromic craniosynostosis. *Semin Plast Surg*, 26(2):64–75, 2012.

[18] 115 apert syndrome. `https://radiologykey.com/115-apert-syndrome/`, 2015. (Last accessed on April 9, 2020).

[19] Ian Bickle. From the case: Pfeiffer syndrome. `https://radiopaedia.org/images/12307746`, 2015. (Last accessed on April 9, 2020).

[20] Jung Won Choi, So Young Lim, and Hyung-Jin Shin. Craniosynostosis in growing children: pathophysiological changes and neurosurgical problems. *Journal of Korean Neurosurgical Society*, 59(3):197, 2016.

[21] Craniosynostosis. `https://www.seattlechildrens.org/conditions/craniosynostosis/#fronto-orbital`. Seattle Children's Hospital, (Last accessed on Feb 20, 2020).

[22] Julia D Sharma, Justine L O'Hara, Alessandro Borghi, Naiara Rodriguez-Florez, William Breakey, Juling Ong, Nu Owase Jeelani, David J Dunaway, and Greg James. Results following adoption of a modified melbourne technique of total scaphocephaly correction. *Journal of Craniofacial Surgery*, 29(5):1117–1122, 2018.

[23] Minimally invasive surgery for craniosynostosis. `https://www.mayoclinic.org/medical-professionals/neurology-neurosurgery/news/minimally-invasive-surgery-for-craniosynostosis/mac-20438762`, 2018. (Last accessed on Feb 20, 2020).

[24] Dong Ha Park and Soo Han Yoon. Craniofacial malformation treatment: craniosynostosis and positional plagiocephaly. *Journal of the Korean Medical Association*, 55(9):878, August 2012.

[25] Distraction osteogenesis. `http://craniofacialteamtexas.com/distraction-osteogenesis/`, 2015. Craniofacial Team of Texas, (Last accessed on April 17, 2020).

[26] Posterior vault expansion. `https://www.gosh.nhs.uk/medical-information/procedures-and-treatments/posterior-vault-expansion`, 2019. The Craniofacial team in collaboration with the Child and Family Information Group, (Last accessed on Feb 20, 2020).

[27] Spring-assisted cranioplasty. `https://www.gosh.nhs.uk/medical-information/procedures-and-treatments/spring-assisted-cranioplasty`, 2019. The Craniofacial team in collaboration with the Child and Family Information Group, (Last accessed on April 14, 2020).

[28] Will Rodgers, Graeme Glass, Silvia Schievano, Alessandro Borghi, Naiara Rodriguez-Florez, Arpan Tahim, Freida Angullia, William Breakey, Paul Knoops, Maik Tenhagen, Justine O'Hara, Allan Ponniah, Greg James, David Dunaway, and NUO Jeelani. Spring-assisted cranioplasty for the correction of nonsyndromic scaphocephaly: A quantitative analysis of 100 consecutive cases. *Plastic and Reconstructive Surgery*, 140:1, 2017.

[29] Craniosynostosis surgery. `https://www.chop.edu/treatments/surgical-treatment-craniosynostosis`. Children's Hospital of Philadelphia, (Last accessed on Feb 20, 2020).

[30] Karan Ramdat Misier, Will Breakey, Lara van de Lande, C. Caron, M. Koudstaal, Silvia Schievano, David Dunaway, Owase Jeelani, and Alessandro Borghi. Using statistical shape modelling to assess outcomes in spring-assisted posterior vault expansion. 2019. Abstarct ISPN.

[31] Alessandro Borghi, Naiara Rodriguez Florez, Federica Ruggiero, Greg James, Justine O'Hara, Juling Ong, Owase Jeelani, David Dunaway, and Silvia Schievano. Assessment of spring cranioplasty biomechanics in sagittal craniosynostosis patients. *Journal of Neurosurgery: Pediatrics*, 20(5):400–409, 2017.

[32] Claes Lauritzen, Yasushi Sugawara, Oya Kocabalkan, and Robert Olsson. Spring mediated dynamic craniofacial reshaping: case report. *Scandinavian journal of plastic and reconstructive surgery and hand surgery*, 32(3):331–338, 1998.

[33] Alessandro Borghi, Naiara Rodriguez Florez, Federica Ruggiero, Greg James, Justine O'Hara, Juling Ong, Owase Jeelani, David Dunaway, and Silvia Schievano. A population-specific material model for sagittal craniosynostosis to predict surgical shape outcomes. *Biomechanics and Modeling in Mechanobiology*, pages 1–11, 2019.

[34] Richard William Francis Breakey, Paul GM Knoops, Alessandro Borghi, Naiara Rodriguez-Florez, Justine O'Hara, Gregory James, David J Dunaway, Silvia Schievano, and NU Owase Jeelani. Intracranial volume and head circumference in children with unoperated syndromic craniosynostosis. *Plastic and reconstructive surgery*, 142(5):708e–717e, 2018.

[35] Jiawen Wang, Donghua Zou, Zhengdong Li, Ping Huang, Dongri Li, Yu Shao, Huijun Wang, and Yijiu Chen. Mechanical properties of cranial bones and sutures in 1–2-year-old infants. *Medical science monitor: international medical journal of experimental and clinical research*, 20:1808, 2014.

[36] Wenyi Yan and Oscar Dwiputra Pangestu. A modified human head model for the study of impact head injury. *Computer methods in biomechanics and biomedical engineering*, 14(12):1049–1057, 2011.

[37] Ying Tan. Chapter 11 - applications. In *Gpu-Based Parallel Implementation of Swarm Intelligence Algorithms*, pages 167 – 177. 2016.

[38] R Merjulah and J Chandra. Classification of myocardial ischemia in delayed contrast enhancement using machine learning. In *Intelligent Data Analysis for Biomedical Applications*, pages 209–235. 2019.

[39] Tomohisa Nagasao, Junpei Miyamoto, Hua Jiang, Tsuyoshi Kaneko, and Tamotsu Tamaki. Biomechanical analysis of the effect of intracranial pressure on the orbital distances in trigonocephaly. *The Cleft palate-craniofacial journal*, 48(2):190–196, 2011.

[40] Imaoka Sheldon. Analyzing viscoelastic materials, mechanical solutions from ansys have convenient tools for calculating deformation of materials in which stiffness changes as a function of loading, time and temperature. *ANSYS Advantage*, 2(4), 2008.

[41] Giavarina Davide. Understanding bland altman analysis. *Biochemia medica*, 25(2):141–151, 2015.

[42] Phoebe Balentyne Diana Mindrila. Scatterplots and correlation. `https://www.westga.edu/academics/research/vrc/assets/docs/scatterplots_and_correlation_notes.pdf`. (Last accessed on May 20, 2020).

[43] Cephalic index. `https://en.wikipedia.org/wiki/Cephalic_index`. (Last accessed on April 17, 2020).

[44] Nikolaos Haliasos, Alessandro Borghi, Mudasir Nazir, Frank Smith, David Dunaway, and Owase Jeelani. Measuring the gosh spring: a mathematical model for the standardization of opening measurements of a novel cranial distraction device. 2014.

[45] Nist/sematech e-handbook of statistical methods. `http://www.itl.nist.gov/div898/handbook/`, 2012. (Last accessed on May 26, 2020).

[46] Least absolute deviations. `https://en.wikipedia.org/wiki/Least_absolute_deviations`, 2020. (Last accessed on May 9, 2020).

[47] Hayes Adam. R-squared definition. `https://www.investopedia.com/terms/r/r-squared.asp`, 2020. (Last accessed on May 26, 2020).

[48] Susan S Margulies and Kirk L Thibault. Infant skull and suture properties: measurements and implications for mechanisms of pediatric brain injury. *J. Biomech. Eng.*, 122(4):364–371, 2000.

[49] David Roylance. Introduction to fracture mechanics. 2001.

[50] E Oterkus, C Diyaroglu, D De Meo, and G Allegri. Fracture modes, damage tolerance and failure mitigation in marine composites. In *Marine Applications of Advanced Fibre-Reinforced Composites*, pages 79–102. 2016.

[51] Ansys, smart fracture. `https://www.ansys.com/-/media/Ansys/corporate/resourcelibrary/whitepaper/smart-fracture.pdf`, 2020. (Last accessed on May 12, 2020).

[52] Alessandro Borghi, Naiara Rodriguez-Florez, Will Rodgers, Gregory James, Richard Hayward, David Dunaway, Owase Jeelani, and Silvia Schievano. Spring assisted cranioplasty: a patient specific computational model. *Medical engineering & physics*, 53:58–65, 2018.

[53] Natario Linard Couser Srivindhya Kolluru. Craniosynostosis syndromes. `https://eyewiki.aao.org/Craniosynostosis_Syndromes`, 2019. (Last accessed on April 9, 2020).